Optical Engineering

SPIEDigitalLibrary.org/oe

Multiband imaging at the diffraction limit using Fresnel x-ray telescopes

Christoph Braig
Peter Predehl

Optical Engineering 51(9), 096501 (September 2012)

Multiband imaging at the diffraction limit using Fresnel x-ray telescopes

Christoph Braig
Friedrich-Schiller-Universität
Institut für Angewandte Physik
Max-Wien-Platz 1, 07743 Jena, Germany
E-mail: christoph.braig@uni-jena.de

Peter Predehl
Max-Planck-Institut für Extraterrestrische Physik
Giessenbachstr. 1, 85748 Garching, Germany

Abstract. We present a diffractive–refractive x-ray telescope for simultaneous imaging in multiple energy bands. Based on segmented achromatic lenses, the system yields an angular resolution around 1 mas between 5 and 10 keV for a focal distance of a few 10^2 km. The total sensitivity, measured via the bandwidth-integrated effective area, reaches at least 10^3 cm^2 keV. Our arrangement exploits Fresnel lenses used in higher phase shift orders for orderly protection from scattered radiation as well as reduced refractive profiles for an enhanced throughput. The telescope, which has its focal plane detector on a separated spacecraft, may be reoriented to new astrophysical targets on short timescales. Scientific applications are briefly discussed for active galactic nuclei. *© 2012 Society of Photo-Optical Instrumentation Engineers (SPIE).* [DOI: 10.1117/1.OE.51.9.096501]

Subject terms: astronomy; diffractive optics; telescopes; x-rays.

Paper 120484P received Apr. 3, 2012; revised manuscript received Aug. 1, 2012; accepted for publication Aug. 2, 2012; published online Sep. 28, 2012.

1 Introduction

Zone plates, Fresnel lenses, and their derivatives have been proposed for next-generation x-ray telescopes and Gamma-ray observatories.[1–4] Those devices can provide an angular resolution at the diffraction limit, down to 10^{-3} arcsec or less, depending on aperture size and energy. However, efficiencies of elementary diffractive lenses are low even for large focal distances, due to an intrinsic linear dispersion in the photon energy. Large-scale segmented versions[5] may provide an acceptable sensitivity but suffer from an extraordinary technical effort. Hybrid optics, designed for a specific energy on behalf of an additional refractive component,[2,6] extend the bandwidth to a few 10^2 eV. In the recent past, a preliminary mission concept[7] found its way to the community and even experimental results on scaled-down versions of Si Fresnel lenses have been published.[8,9]

Despite their impressive optical capabilities with respect to resolution as well as sensitivity, all those telescopic arrangements are restricted to a specific energy band. In view of potential scientific applications, ranging from spectrally to time resolved observations of dynamical, complex x-ray emitting processes, new insights are expected from the simultaneous imaging in several spectral regions. Only two-band achromatic x-ray telescopes for measurements of, for instance, hardness ratios have been introduced so far.[10,11]

In this paper, we develop an improved compact achromatic instrument designed for five energy windows, each a few 10^2 eV in width. Based on simple geometrical considerations, constraints to aperture radii and detector sizes are analyzed in Sec. 2. Theoretical aspects of segmented apertures and stepped hybrid lenses are treated in the next chapter. Optimized in terms of sensitivity in Sec. 4, these concepts will be applied to a specific design, and its optical properties will be evaluated in Sec. 5. The focal plane is investigated in Sec. 6. In Sec. 7, applications to several classes of x-ray targets on various angular scales in general and active galactic nuclei (AGN) in particular are picked out for illustration. Conclusions and an outlook to further steps will be given afterward.

2 Nested Hybrid Ring Lenses

Diffractive lenses, as they are known in the literature, span a variety of focusing grating structures with different profiles, not only in the x-ray band. Their optical properties are mainly determined by that specific profile type and will be exploited in this work, to enable an efficient multiband imaging system. In particular, our concept relies on blazed "Fresnel lenses" rather than more conventional binary "zone plates." The terminology is clarified in Appendix A. In the x-ray band, such blazed profiles may be operated in higher "phases shift orders," as it is also reviewed in Appendix A. Moreover, Sec. C of this appendix contains a sorted list of symbols and conventions, as they are used within the text.

An achromatic diffractive–refractive x-ray lens consists of a diffractive (Fresnel) lens with a focal length F_Z and a diverging, i.e., convex refractive component with a focal length $F_L = -2F_Z$ in close contact.[2] Figure 1 gives an impression of that scheme. As it can be shown,[6] this combination provides indeed the most effective correction of the chromatic aberration far away from electronic resonances, where the quite different dispersion of the diffractive ($F_Z \propto E$) and refractive lens ($F_L \propto E^2$) is exploited for compensation.

Conventional diffraction-based transmissive single-band instruments of that type use their whole aperture for focusing photons of an energy E_0. Such optics are characterized by a grating period strictly constant in r^2, where r is the lens radius. In contrast, dual- or even multiband versions should be composed of individual ring lenses for all energy bands E_i, structured properly with respect to their grating periods,[10,11] and blazed for an optimized efficiency. Since Fresnel lenses exhibit peculiar multiorder diffraction properties in the x-ray regime,[12] an appropriate geometrical arrangement of the nested set of ring lenses is essential in order

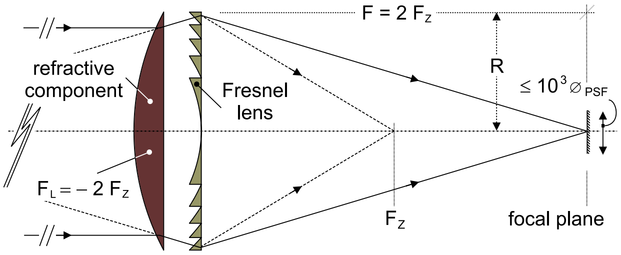

Fig. 1 Hybrid lens of radius *R* for dispersion-corrected x-ray imaging. The diffractive and refractive components are abbreviated by the subscripts *Z* and *L*. $\varnothing_{\mathrm{PSF}}$ denotes the focal spot size; the detector may contain typically $\leq 10^3$ resolution elements ($\varnothing_{\mathrm{PSF}}$) across its diameter.

to protect the detector in the focal plane from any scattered stray light.[10]

2.1 *Achromatic Multiorder Fresnel Diffraction*

We assume that the partial lenses for all energies E_i are blazed on a global reference energy E_0 and differ only by their grating period. Let $F_i^{(Z)}(E_0)$ denote the corresponding focal lengths of the diffractive lens components associated with E_i in their 1st phase shift order, if the lens would be operated at E_0. As it was mentioned above, the focusing properties of hybrid lenses rely on the focal length dispersion of the diffractive (Z) and the refractive (L) component as well. The former one fulfills

$$z_{m_i}^{(Z)}(E_i) = \frac{1}{m_i} F_i^{(Z)}(E_0)\frac{E_i}{E_0}, \tag{1}$$

because the focal distance $z_{m_i}^{(Z)}$ of diffractive devices scales proportional to E_i. If E_i is an integer fraction of E_0, i.e., $E_i = m_i^{-1}E_0$ with $m_i \epsilon \mathbb{N}$, the actual focal position $z_{m_i}^{(Z)}(E_i)$ would be reduced by the factor m_i^2 with respect to the nominal 1st order focus for E_0. This unique feature of x-ray Fresnel lenses relies on the inverse squared dependence of the refractive phase shift in the lens material from the photon energy[5] and enables their simultaneous usage in several discrete energy bands with an ultrahigh efficiency, only constrained by the—often low—absorption. For distinct low-Z materials like li(thium) and be(ryllium), the losses are almost negligible, indeed in the spectral range beyond ∼5 keV at least. In particular, the efficiency of an absorption-affected Fresnel lens in order m_i can be written using the "critical zone number" N_0[13] as

$$\hat{P}_{m_i}(E) = \frac{1 - 2e^{-\frac{1}{N_0}\frac{E_0}{E}}\cos(2\mathcal{G}_{m_i}(E)) + e^{-\frac{2}{N_0}\frac{E_0}{E}}}{4\mathcal{G}_{m_i}^2(E) + (E_0/N_0E)^2}, \tag{2}$$

with $\mathcal{G}_{m_i}(E) \equiv \pi(m_i - E_0E^{-1})$[12] and $N_0(E) \equiv \delta(E)/2\pi\beta(E)$ for the complex refractive index $n = 1 - \delta - i\beta$. An approximative, but more "handy" representation of Eq. (2) separates the absorption-related contribution $\mathcal{U}_{m_i}^{(Z)}(E)$ from the Fresnel-diffractive term $\hat{P}_{m_i}^{(0)}(E)$, as it is further discussed in Appendix B:

$$\hat{P}_{m_i}(E) \approx \mathcal{U}_{m_i}^{(Z)}(E) \times \hat{P}_{m_i}^{(0)}(E), \tag{3}$$

where $\hat{P}_{m_i}^{(0)}(E)$ denotes the lossless sinusoidal function

$$\hat{P}_{m_i}^{(0)}(E) = \mathcal{G}_{m_i}^{-2}(E)\sin^2[\mathcal{G}_{m_i}(E)], \tag{4}$$

as it can be directly derived for the limit $N_0 \to \infty$.[5] The multiplicative term $0 < \mathcal{U}_{m_i}^{(Z)}(E) < 1$ describes the fraction of the transmitted light around E_i, which is actually diffracted in the order m_i. For an absorbing Fresnel lens, this fraction is found as somewhat less than 100%, since the nonuniform transmission profile scatters some radiation of the same energy into other orders neighbored to m_i—now in the sense of the classical "diffraction order" again. In the "lower harmonics" $E = m_i^{-1}E_0$, we find $\hat{P}_{m_i}^{(0)}(E_i) \to 1$ and the net efficiency $\hat{P}_{m_i}(E_i)$ will reach its maximum

$$\mathcal{U}_{m_i}^{(Z)}(E_i) = (m_i^{-1}N_0)^2[1 - \exp(-m_iN_0^{-1})]^2, \tag{5}$$

where the value of N_0 is taken at E_i. Equation (2) or—more clearly—Eq. (4) implies that the Fresnel lens still works in the intermediate range between two energies E_i and $E_{i\pm1}$, albeit with an efficiency less than that described by Eq. (5).[5,10] In this case, the x-rays are diffracted into several, mainly neighbored orders less and greater than m_i, where the fraction that remains in m_i is given by Eq. (4). This effect is similar to that caused by absorption from above, but the origin is different, since the phase condition $\Delta\phi = 2m_i\pi$ is violated now. However, the detector used within this work is assumed to resolve and select the (achromatic) energy bands around E_i within their relatively narrow diffraction-limited spectral width where $\hat{P}_{m_i}^{(0)}(E) \lessapprox 1$ and the power that is diffracted into orders neighbored to m_i due to this phenomenon is assumed to be quite small. Figure 2 demonstrates the multiple phase shift order properties schematically for one Fresnel groove, where the color density visualizes the absorption.

In contrast to the linear dispersion of diffractive lenses from Eq. (1), refractive x-ray lenses follow far away from atomic absorption edges an even stronger energy dependence—albeit without intrinsic multiorder properties,

$$z_{m_i}^{(L)}(E_i) = F_i^{(L)}(E_0)(E_i/E_0)^2. \tag{6}$$

This function is based on the relation $\delta(E) \propto E^{-2}$. The combination of a diverging refractive with an ordinary focusing diffractive component leads to achromatic compensation. The focal position $z_{m_i}(E)$ of such a corrected hybrid lens for a given energy E in the vicinity of E_i in the phase

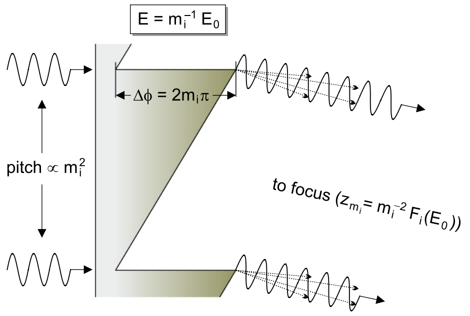

Fig. 2 Multiorder diffraction from Fresnel lenses. For energies $E = m_i^{-1}E_0$, an almost 100% efficiency is reached in a focal distance $z_{m_i} \propto m_i^{-2}$, apart from small losses into neighbored orders (gray arrows) due to absorption. The common focus concept is realized with an adapted pitch $\propto m_i^2$ in the nested ring lens configuration.

shift order m_i due to the diffractive–refractive dispersion can be found from the basic geometrical imaging formula for a thin-lens doublet. With the focal length $F_i(E_0) = -F_i^{(L)}(E_0)$, we find[6]

$$\frac{z_{m_i}(E)}{F_i(E_0)} = \left(2m_i - \frac{E_0}{E}\right)^{-1} \frac{E}{E_0}. \tag{7}$$

It should be emphasized that, in agreement with the features of the pure diffractive lens, the dispersion compensation only works indeed within a certain spectral band around the distinct energies E_i, i.e., $E \approx E_i$. In Fig. 3, the dispersion properties of both dispersion-compensated and solely diffractive optics are shown for the higher-order scheme on which the current work is based.

In coincidence with Eq. (3), the maximum efficiency is obtained around the harmonic energies $E_i = m_i^{-1} E_0$. In practice however, it will be significantly modified by the strong absorption in the "thick" refractive lens. For convenience, we identify these discrete, infinitely sharp energy values E_i with the achromatic spectral bands $\Delta E_A^{(i)}$ in their vicinity from now on, if not stated differently. The energy-dependent, purely refractive transmission $\mathcal{T}_{m_i}(E_i)$ in an achromatic system separates from the Fresnel contribution $\hat{P}_{m_i}$ again. The total fraction $\mathcal{P}_{m_i}(E_i)$ of the incident power that is focused into the phase shift order m_i is then given as

$$\mathcal{P}_{m_i}(E_i) = \langle \hat{P}_{m_i}(E) \rangle_{\Delta E_A^{(i)}} \times \mathcal{T}_{m_i}(E_i) \tag{8}$$

with $0 < \mathcal{T}_{m_i}(E_i) < 1$. In Eq. (8), the diffractive efficiency $\hat{P}_{m_i}(E)$ was averaged over the achromatic bandwidth $\Delta E_A^{(i)}$, which will be defined in detail in Sec. 4. This mean accounts for the sinusoidal energy dependence from Eq. (4) and will typically reduce the efficiency by a few percent with respect to the maximum $\mathcal{U}_{m_i}^{(Z)}(E_i)$ from Eq. (5). For a relatively small and effectively negligible absorption in the diffractive component with $\mathcal{U}_{m_i}^{(Z)} \to 1$, the total hybrid lens transmission—and hence its efficiency around E_i is only determined by the massive refractive profile structure. As opposed to $\hat{P}_{m_i}$, the refractive transmission will average itself over the achromatic band, since it increases approximately linear with the energy on a typical scale of only a few 10^2 eV. $\mathcal{T}_{m_i}(E_i)$ depends on the energy and the phase shift order and will be used again in Sec. 4, to derive and analyze the lens design.

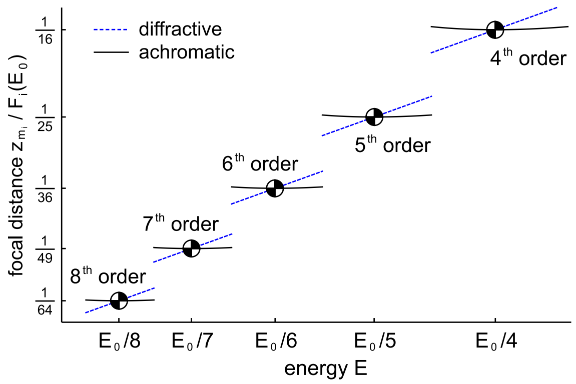

Fig. 3 Diffractive (blue dotted) and achromatic (black straight) focal length dispersion as a function of the fractional energy E for the five orders $4 \leq m_i \leq 8$ in use. The focal distance z_{m_i} is normalized to $F_i(E_0)$.

As it follows from Eq. (4), $\mathcal{P}_{m_i}(E_i)$ exhibits local, exclusive peaks with an almost constant as dispersion-corrected efficiency near $\mathcal{T}_{m_i}(E_i)$ for suitable low-Z materials at integer fractions of the basic energy E_0, i.e.

$$\mathcal{P}_{m_i}(E_i) \to \mathcal{T}_{m_i}(E_i) \Leftrightarrow E_i = m_i^{-1} E_0. \tag{9}$$

This feature permits the design of a common focal distance, achromatic instrument for several energy bands in analogy to former two-band versions.[10] We assume an arrangement of annular, nested lenses. Each one will be assigned to one specific energy E_i, and their diffractive Fresnel components will have the same thickness but a different grating period or "pitch," according to Fig. 2. In this way, the focal distance z_{m_i} of each ring lens can be adapted for coincidence in the common focal plane at $z = F$. In particular, the boundary condition of this universal "working" focal length F for all spectral bands with index i and their individual 1st order focal lengths $F_i(E_0) \geq F$ reads as

$$F = z_{m_i}(E_i) = \text{const.} \Leftrightarrow F_i(E_0) = m_i^2 F, \tag{10}$$

for each energy $E_i \leq E_0$. Here, we assume that the corresponding hybrid ring lens is used in its dedicated phase shift order $m_i \geq 1$, defined via $E_i = m_i^{-1} E_0$. As it was described above by Eqs. (3) and (5), the Fresnel lens provides a very high efficiency up to 100% at these energies E_i, only limited by absorption. This feature does not contradict the established (blaze) grating theory[14] but rather adds that "new" phenomenon of the phase shift order as the special condition, under which the most efficient diffraction will occur in a Fresnel x-ray lens. That is, every band E_i represents in our nested lens arrangement one certain phase shift order m_i in which the dedicated Fresnel ring lens with its universal blaze energy E_0 is operated. Hence, the energies E_i which can be actually used for imaging in the telescope are at most as large as E_0 but normally smaller, to obtain closely spaced energy values E_i, as it will be demonstrated in Sec. 5 for five bands within 5 and 10 keV (Fig. 3).

2.2 *Stray Light Protection*

On the other hand, each annular aperture is still constricted to a certain spectral band. We consider two energy bands from the set $\{E_i | 4 \leq i \leq 8\}$. The same lens component that focuses photons of an energy E_i to the common focal distance F, will thus diffract other x-rays with $E_j \neq E_i$ to another axial position $z_{m_j}(E_j)|_{E_i}$, which depends on the ratio between E_i and E_j: In analogy to Eq. (10), we find

$$z_{m_j}(E_j)|_{E_i} = m_j^{-2} F_i(E_0) \quad \text{in order } m_j. \tag{11}$$

For convenience, this axial position will be normalized from now on by means of the dimensionless quantity ζ_{ij},

$$\zeta_{ij} \equiv F^{-1} z_{m_j}(E_j)|_{E_i} \to \zeta_{ij} = (m_i/m_j)^2. \tag{12}$$

Depending on which of the two involved orders is higher, ζ_{ij} may take values less or greater than 1. From Eqs. (9) and (12), the relation

$$\psi_{ij} = \sqrt{\zeta_{ij}} \quad \text{with } \psi_{ij} \equiv E_j / E_i \tag{13}$$

is obtained, where the normalized energy ψ_{ij} was defined in analogy to ζ_{ij} for energies E_j which are focused by the ring lens dedicated to E_i.

In the common focal plane, the diffracted wave front for $E_j \neq E_i$ would be therefore strongly blurred rather than sharply imaged. The ring-shaped nature of the aperture for E_i implies an annular scattering halo of photons with that energy E_j around the detector. Such detuned x-rays must hold a distance of at least $2r_{\mathrm{FOV},j}$ from the optical axis in the focal plane, in order to avoid any contamination over the whole field of view (FOV).

Here, we assume an individual sensitive detector radius $r_{\mathrm{FOV},j}$ for each energy E_j. According to the theorem on intersecting lines, an obstruction $0 < a_i < 1$ must be applied for sufficient protection to the partial Fresnel lens of radius R_i, operating at E_i. As it was discussed in detail elsewhere,[10] the smallest possible value for a_i can be described by the "shadow factor"

$$\mathcal{S}(\zeta_{ij}) \equiv \pm 2(1 - \zeta_{ij}^{-1})^{-1} \quad \text{with } \mathcal{S}(\zeta_{ij}) > 0. \tag{14}$$

Using Eq. (14), we find the lowest possible obstruction of the lens component for E_i as a function of $r_{\mathrm{FOV},j}$,

$$a_i R_i \geq \mathcal{S}(\zeta_{ij}) r_{\mathrm{FOV},j} \quad \text{or} \quad a_i R_i \geq \pm \frac{2 r_{\mathrm{FOV},j}}{1 - \psi_{ij}^{-2}}. \tag{15}$$

The algebraic sign (±) distinguishes between "red" and "blue" detuned radiation—following ζ_{ij}, it is chosen such that $\mathcal{S}(\zeta_{ij}) > 0$. Figure 4 illustrates the geometrical relations for one ring lens only, to simplify the presentation. For each combination of energies (E_i, E_j), the lower limits to the absolute inner radii $a_i R_i$ can be calculated now from Eq. (15) in units of the detector radius $r_{\mathrm{FOV},j}$. Obviously, the condition is only determined by the ratio ψ_{ij} and would show a singularity if $i = j$. In Table 1, the required (minimum) obstructions for multiband versions from the 4th up to the 8th phase shift order are listed. Quite different energies like $(\frac{1}{4}E_0, \frac{1}{7}E_0)$—abbreviated to (E_4, E_7) from now on—or (E_5, E_8) yield $a_i R_i \approx r_{\mathrm{FOV},j}$. In contrast, the highest ratios $a_i R_i / r_{\mathrm{FOV},j}$ arise for $E_i \approx E_j$ with $i = j \pm 1$. The inner lens radius $(a_i R_i)_\bullet$ that should be finally applied in the nested telescope is given as the largest value from Eq. (15) with respect to $E_j \neq E_i$,

$$(a_i R_i)_\bullet \equiv \max_{j \neq i} [\mathcal{S}(\zeta_{ij}) r_{\mathrm{FOV},j}]. \tag{16}$$

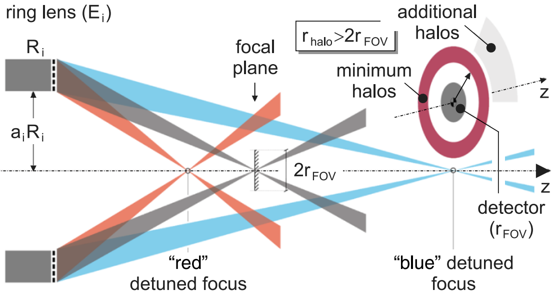

Fig. 4 Light cones for focused (gray) and "red" ($E_j < E_i$) and "blue" ($E_j > E_i$) detuned x-rays, imaged by an annular aperture. The inset (upper right) shows superimposed minimum (purple) and outer (light gray) halos.

Table 1 Obstructions of multiband apertures.

Radii	$r_{\mathrm{FOV},8}$	$r_{\mathrm{FOV},7}$	$r_{\mathrm{FOV},6}$	$r_{\mathrm{FOV},5}$	$r_{\mathrm{FOV},4}$
$a_8 R_8$	—	**128/15**	32/7	128/39	8/3
$a_7 R_7$	98/15	—	**98/13**	49/12	98/33
$a_6 R_6$	18/7	72/13	—	**72/11**	18/5
$a_5 R_5$	50/39	25/12	50/11	—	**50/9**
$a_4 R_4$	2/3	32/33	8/5	**32/9**	—

Bold values indicates the numerical results.

The numerical results of that condition for $4 \leq i,\ j \leq 8$ are typed in bold in Table 1. For the simplest case of a universal detector size $2r_{\mathrm{FOV}}$ for all energy bands, the optimized obstructions are shown in Fig. 5 once more. We will use that set of orders and the obstructions from Fig. 5 in Sec. 5 for the design of the prototype multiband telescope.

Compared to former two-band lenses operated in the 1st phase shift order,[10] the usage of higher orders is clearly advantageous: To illustrate the difference, we select the two bands E_6 and E_8 from above, related as $E_6 = \frac{4}{3}E_8$. Since we have now $m_i = 1$ for both of them, Eq. (7) would lead to $\zeta_{86} = 16/15$, if E_8 is identified with E_0 and vice versa, $\zeta_{68} = 9/8$, if E_6 plays the role of the basic energy. The associated obstructions are found from Eq. (15) as $32 r_{\mathrm{FOV},6}$ and $18 r_{\mathrm{FOV},8}$, respectively—much more than the inner ring diameters $\approx 4.6 r_{\mathrm{FOV},6}$ and $\approx 2.6 r_{\mathrm{FOV},8}$ from Table 1 for the higher-order scheme. Hence, this new approach allows for an enlarged effective area and/or FOV in all incorporated bands.

The largest, i.e., most critical obstructions in Table 1 arise for $\zeta_{ij} \approx 1$ with a maximal $\mathcal{S}(\zeta_{87}) \approx 8.5$ in that set of energies, wherefore $m \lesssim 8$ may be considered as an upper limit to the range of usable orders. On the other hand, lower orders (i.e., the 1st, 2nd, and 3rd one in our case) may be simply added in the center of the aperture.

In contrast to the wave diffraction theory on which the rest of the work within this article is based, the stray light protection as introduced above is considered on an elementary geometrical level. There are good reasons to choose this simplified picture here: First, diffraction effects from the limited aperture size—effectively the segments' dimension (Sec. 3)—would arise on the milli-arcsec scale and can be neglected, since only the outermost edge of the sensitive

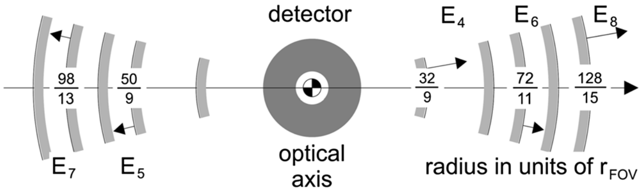

Fig. 5 Optimal shadow function $\mathcal{S}(\zeta_{ij})$ of the nested lens aperture taken from Table 1 in units of the detector radius r_{FOV} for the five energy bands E_i with $4 \leq i \leq 8$.

detector plate, if any, would be affected by that subtle deviation from the geometrical shadowing. Second—and this is the more sophisticated argument—we assume that the detector is able to discriminate the achromatic spectral bands around E_i from closely neighbored energies by its inherent resolution. Outside their diffraction-limited intrinsic bandwidth ΔE (Sec. 4), x-ray lenses of all types would produce a blurred focal spot—a doughnut-like PSF is typical, for instance, when an annular lens is used in the close vicinity with $E \approx E_i$ outside the bandwidth ΔE. Such effects need to be avoided obviously, to maintain the diffraction-limited performance. In our scheme, however, the energies of interest from the spectral set $\{E_i | 4 \leq i \leq 8\}$ are separated from each other by several 10^2 eV or even keV. Now far beyond the Rayleigh length, the Gaussian doughnut shape will effectively approach the shadow cone from Fig. 4. This effect is even more enhanced by the multiorder arrangement that diffracts those distinct energies $E_j \neq E_i$ into particularly distant focal positions according to Eq. (12). Hence, the geometrical picture is clearly justified in this regime and greatly simplifies the formal description of the stray light protection scheme.

3 Segmented Apertures

Implemented in meter-scaled but compact, i.e., coherent lenses, the separation between the two spacecraft would reach several 10^3 or even 10^4 km. Such long focal distance telescopes suffer from the drawback of severe fuel consumption for the reorientation to new targets, despite their high sensitivity and angular resolution.[2] An appropriate lift-off of large-scale objectives seems challenging, moreover. We thus propose a segmented lens design for transport reasons and for the sake of a significantly reduced focal length.[5,6] Within this section, we omit the index i for simplicity; the results are valid for each energy E_i.

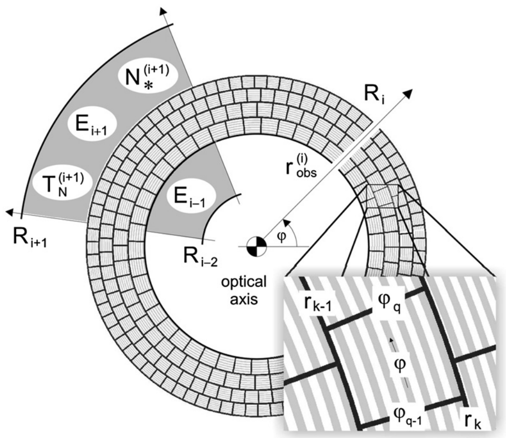

Fig. 6 Segmentation scheme of transmissive lenses. Only one single ring lens for E_i is shown in detail. Alternating white/gray rings indicate Fresnel zones, black lines show radial (φ_q) and annular (r_k) segment boundaries.

3.1 *Geometrical Rules of Annular Segmentation*

Naturally segmented into fields of a constant Fresnel zone number $N_\star$, we get $T_N = N/N_\star$ rings the aperture (N zones) is divided in. Radial cuts approximate the segments to squared lens sections for sufficiently large ring numbers $1 \leq k \leq T_N$. In general, for an aperture radius R and integers rounded by $x \to [x]$, the annular boundaries $r_k = (k/T_N)^{1/2}R$ are complemented by the radial cuts $0 \leq \varphi_{k,q} < 2\pi$ with a random phase rand_k via

$$\varphi_{k,q} = \mathrm{rand}_k + 2\pi(q-1)\left\{\pi\frac{\sqrt{k}+\sqrt{k-1}}{\sqrt{k}-\sqrt{k-1}}\right\}^{-1}, \tag{17}$$

as illustrated in Fig. 6. If randomly shifted in radial direction within about ± one mean zone width of the corresponding ring, all individual, optically independent segments within this ring contribute incoherently to the focal intensity distribution, i.e., the overall point spread function (PSF). In achromatic lenses, its half-energy width (HEW) is affected by a nonuniform absorption across the refractive segmented thickness profile $h_k(r)$. This transmission gradient is sketched in Fig. 7 by the red-scaled cross-section. We neglect the diffractive thickness and obtain with the 2π-thickness $h_{2\pi} \equiv \lambda/\delta(\lambda)$ the profile

$$\left(\frac{1}{h_{2\pi}}\right)h_k(r) = \frac{N}{4}\left[\frac{k}{T_N} - \left(\frac{r}{R}\right)^2\right]. \tag{18}$$

It should be noted that the maximum thickness of each segment is the same within one of the five nested ring lenses, due to $N_\star = \text{const.}$—in contrast to an alternative design as proposed by Umbach.[15] For sufficiently large ring numbers T_N, the segment profiles approximate the shape of prisms whose effective zone number is virtually increased to $m \times N_\star$ when the lens is operated in the m'th phase shift order (Fig. 7).

In the strong absorption regime with $mN_\star \gg N_0$, one might expect an improved performance for an additional coherent reduction ("stepping") of each segment, as shown in Fig. 8. Coherently reduced refractive components enhance the transmission on the price of a much more complicated spectral response.[2,10] As a consequence of the lower absorption gradient, however, stepped segments can conserve their inherent angular resolution—defined by the corresponding segment size—to a great extent. In general, the coherent profile reduction is characterized by an integer w, which describes the number of refractive saw-tooth steps within one segment.

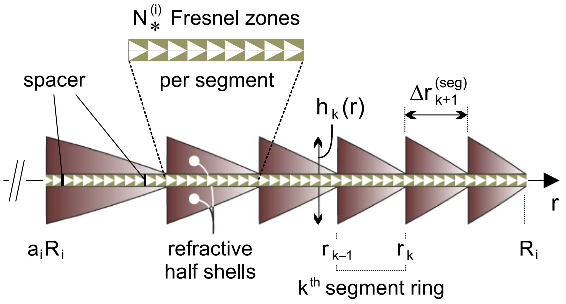

Fig. 7 Cross-section through a segmented ring lens with radii a_iR_i and R_i. The diffractive Fresnel lens (upper graphics) is included within the refractive component (green central region). Spacers (black) protect the Fresnel profiles from self-damage. For simplicity, only six optically independent massive segments ($w = 1$) are shown.

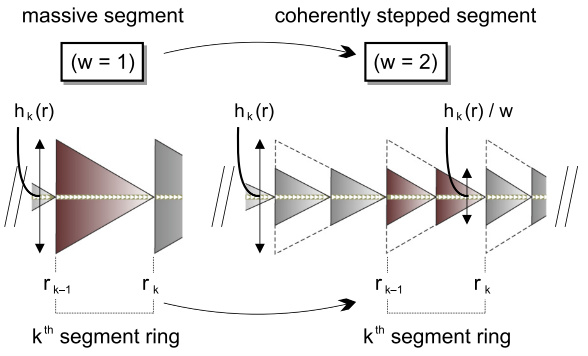

Fig. 8 Coherent stepping of massive segments. On the left, the cross-section through the k'th segment ring ($w = 1$) is shown. On the right, this segment is coherently reduced with two "teeth" or $w = 2$ (highlighted in dark red).

3.2 *Absorption-Affected Resolution*

Since the transmission within one segment depends on the thickness $h_k(r)$ and therefore on the radius r according to Eq. (18), we expect an expanded HEW $\varnothing_{\mathrm{PSF}}$ of the PSF compared to the virtual analogue of a segment of equal size without absorption:

$$\varnothing_{\mathrm{PSF}} = Q_w(s)\varnothing_{\mathrm{PSF}}^{(0)} \quad \text{with } s \equiv (mN_\star)/N_0, \tag{19}$$

where the superscript "0" denotes the spot size of an ideal segment without absorption ($s \to 0$). The parameter $Q_w(s)$ increases monotonically with s and has been calculated by Fourier transformation of rotated segments.[10]

Table 2 lists the spatial resolution $Q_1(s)$ for massive ($w = 1$) segments with s-ratios up to 9, normalized to the absorption-free case. If the segments are stepped coherently as shown in Fig. 8, much larger s-ratios are possible. In Table 3, the normalized resolution $Q_w(s)$ is listed for the parameters $w = 4$ and $w = 5$ as they will be used in Sec. 5.

If we neglect the small nonuniformity of the periodic absorption within the diffractive lens component, the mean angular resolution (HEW) of one segmented ring lens as in Fig. 6 results from all superimposed single-segment PSFs of varying lateral dimension. The incorporation of all factors[5,10] leads to a linear relationship between the angular resolution of an ideal, transparent aperture with radius R and an obstructed, segmented hybrid lens:

$$\Delta\epsilon_{\mathrm{inc}} = \eta_N(a)T_N Q_w(s)\Delta\epsilon_{\mathrm{coh}}, \tag{20}$$

with $\Delta\epsilon_{\mathrm{coh}} = \alpha\lambda R^{-1}$ and $\alpha = 0.535$ for the conversion from coherent ($\Delta\epsilon_{\mathrm{coh}}$) to incoherent angular resolution ($\Delta\epsilon_{\mathrm{inc}}$). The parameter $\eta_N(a)$ depends on the central obstruction a and is listed in Table 4. Using Eq. (20), $T_N = N/N_\star$ from above and the fundamental equation $R^2 = (N/2)\lambda F$ for an achromatic lens, the spot size $\varnothing_{\mathrm{PSF}}$ and the aperture radius R of ring lenses with zone numbers $N_\star$ are related via $\Delta\epsilon_{\mathrm{inc}} = \varnothing_{\mathrm{PSF}}/F$ as

$$\varnothing_{\mathrm{PSF}} = 2\alpha\eta_N(a)(mN_\star)^{-1}RQ_w(s). \tag{21}$$

Table 2 Resolution of massive segments ($w = 1$).

s	1.00	2.00	3.00	4.00	5.00	6.00	7.00	8.00	9.00
Q_1	1.00	1.01	1.03	1.06	1.09	1.12	1.17	1.21	1.27

Table 3 Resolution of stepped segments ($w \geq 2$).

s	4.00	8.00	12.0	16.0	20.0	24.0	28.0	32.0	36.0
Q_4	1.00	1.02	1.04	1.06	1.10	1.15	1.20	1.27	1.36
Q_5	1.00	1.01	1.02	1.04	1.06	1.09	1.13	1.17	1.22

In principle, the absorption modifies the shape of the PSF, not only its HEW diameter, and hence the central obstruction a should also enter the correction $Q_w(s)$: According to Fig. 6, the size of the segments decreases toward larger radii, whereas their transmission gradient—i.e., the difference between maximum and minimum transmission within one segment—is kept constant within one ring lens for E_i, due to the constant thickness $h_k(r)$ of the refractive prism-like profile (Fig. 7).

Since all those segments contribute a diffraction pattern of the same shape but with a different, k-dependent HEW to the incoherent PSF in the focal plane, that resulting PSF increases both with absorption and toward larger central obstructions. Strictly spoken, the effects of both influencing factors on the superimposed intensity pattern are not independent from each other, and the incoherent PSF would have to be calculated by an explicit Fourier transformation of the full aperture. An extremely time-consuming numerical effort usually forbids that way in practice. So, a convenient approach may separate the absorption-induced enlargement of the focal spot size from the purely geometrical effect of varying segment sizes. As it was shown in detail previously[6] by an explicit comparison with the results of a direct numerical integration, the errors of such an approximative factorization into $\eta_N(a)$ and $Q_w(s)$ as in Eq. (21) range in the order of a few percent or less, independent of T_N.

In this way, Eq. (21) permits the calculation of the spatial and angular resolution for one distinct energy E_i, i.e., an isolated ring lens (Fig. 6) within the nested aperture. The integration of a segmented multiband telescope implies an additional degree of complexity, however, since both the common focal distance condition and the resolution/efficiency requirements need to be fulfilled for all spectral bands. This task will be solved in the next section.

4 Optimization of the Photon Throughput

We assume a circular detector plate that contains $n_{\mathrm{FOV},j} = 2r_{\mathrm{FOV},j}/\varnothing_{\mathrm{PSF}}^{(j)}$ resolution elements in diameter, different for each energy E_j in general. With this relation, Eq. (15) reads as

Table 4 Correction for central obstruction.

a	0.0	0.1	0.2	0.4	0.6	0.8	1.0
η_N	2.27	2.30	2.35	2.55	2.86	3.19	3.55

$$a_i R_i \geq \frac{1}{2} \mathcal{S}(\zeta_{ij}) \varnothing_{\mathrm{PSF}}^{(j)} n_{\mathrm{FOV},j} \quad \text{with } i \neq j. \tag{22}$$

The focal spot size from Eq. (21), written for the energy E_j, can now replace that quantity in Eq. (22): we obtain from Eq. (21) the expression

$$m^{(j)} N_\star^{(j)} \varnothing_{\mathrm{PSF}}^{(j)} = 2\alpha \eta_N(a_j) R_j Q_w(s_j), \tag{23}$$

using the generalized zone ratio $s_j \equiv m^{(j)} N_\star^{(j)} / N_0^{(j)}$. The—logical or formal—combination of the lower limit to $a_i R_i$ from Eqs. (22) with (23) leads to an implicit inequality for the allowed effective zone numbers $m^{(j)} N_\star^{(j)}$ in each energy band E_j. We find

$$m^{(j)} N_\star^{(j)} \geq \alpha \mathcal{S}(\zeta_{ij}) \frac{R_j}{R_i} n_{\mathrm{FOV},j} \frac{\eta_N(a_j)}{a_i} Q_w(s_j). \tag{24}$$

There is no stringent strategy for the evaluation of Eq. (24) as it relates the lens design constraints for the imaged energy E_i to the stray light protection conditions for $E_j \neq E_i$. In fact, the inequality Eq. (24) must be solved numerically for reasonable values of the central obstruction $a_{i,j}$ and the ring lens radius $R_{i,j}$ as well as an acceptable number $n_{\mathrm{FOV},j}$ of resolvable focal spots within the detector diameter. In practice, all zone numbers are set close to that limit; i.e., the lowest possible $N_\star$ is chosen in order to maximize the efficiency, as long as the focal spot diameters fulfill the technical demands. Another interesting aspect of that relation should be recognized: Inequality Eq. (24) not only states the geometrical conditions for an appropriate choice of the annular aperture dimensions for disjunct phase shift orders $i \neq j$ but includes implicitly the imaging characteristics in terms of the focal spot size as well. Since the spatial resolution is dependent on the dominant absorption in the refractive lens component via $Q_w(s_j)$, this energy- and material-dependent transmission affects the determination of reasonable effective zone numbers $m^{(j)} N_\star^{(j)}$ as well. From that point of view, it is also clear that an eventual nonnegligible absorption in the diffractive component can be actually ignored in that special context: Because of $m^{(j)} N_\star^{(j)} \ggg 1$, the Fresnel lens with its near-uniform transmission will not degrade the spatial resolution, i.e., its corresponding Q-factor would be virtually identical to 1.

4.1 *Effective Area and Spectral Bandwidth*

The optical performance of an (x-ray) telescope is not only determined by its angular resolution but also by its sensitivity. In the case of conventional Wolter mirror telescopes, this quantity is usually measured as the effective area within a certain range of several keV. Fresnel-type lenses are limited to a narrow spectral band of a few eV or less, due to their inherent focal length dispersion. For achromatic optics, however, an increased sensitivity is expected in relation to the sole diffractive analogue, despite the strong absorption in the refractive correction component (Fig. 1). For a flux of the astronomical target measured in photon count rates rather than erg $\sec^{-1}$, we calculate the "luminous power" $A_{\mathrm{eff}} \times \Delta E$ for an effective area A_{eff}, usable within the diffraction-limited spectral bandwidth ΔE. Expressed in units of ($\mathrm{cm}^2\,\mathrm{keV}$), the sensitivity of such diffractive optics becomes assimilable with that of mirror-based missions like Chandra or XMM-Newton, if their effective area is integrated over the detectable energy range of interest.

In the following, we neglect temporarily the phase shift order index i for simplicity. For one segmented ring lens from above, the effective area can be calculated from

$$A_{\mathrm{eff}} = \pi (R_{\max}^2 - R_{\min}^2) \langle \hat{P}(E) \rangle_{\Delta E_A} \mathcal{T}_w(s), \tag{25}$$

where $R_{\min}$ and $R_{\max}$ describe the inner and outer radii of the annular aperture, respectively. The mean diffractive efficiency $\langle \hat{P}(E) \rangle_{\Delta E_A}$ is taken from Eq. (8). On the other hand, the refractive contribution to the transmission through that ring lens is given as

$$\mathcal{T}_w(s) = 2s^{-1} w \{1 - \exp[-(s/2w)]\}, \tag{26}$$

which approximately coincides with the total transmission, if the absorptive contribution from the diffractive component can be neglected. The diffraction-limited bandwidth ΔE needs further consideration: In the case of purely diffractive optics with $N_\star$ geometrical Fresnel zones per segment in 1st order, we used[5]

$$\Delta E_Z = (m N_\star)^{-1} E. \tag{27}$$

The overall bandwidth of the dispersion-corrected achromatic segmented lens is enlarged to[11]

$$\Delta E_A^{(w)} = 2(\mathrm{wm}^{-1} / N_\star)^{1/2} E \quad \text{with } w \epsilon \mathbb{N}, \tag{28}$$

where w denotes the number of (coherent) steps within one segment.[10] For an unstepped segment with $w = 1$, Eq. (28) reduces to the well-known[6] expression

$$\Delta E_A^{(1)} = 2(m N_\star)^{-1/2} E. \tag{29}$$

For $w \geq 2$, a regular comb structure of well-focused energies rather than the full corrected band is detected in the focal plane. Figure 9 illustrates the spectral response for both cases. In particular, within the spectral band given by Eq. (28), the peaks are defined by the condition $N_\star (4w)^{-1} \epsilon \mathbb{N}$ and separated by an equidistant spacing of $4w(mN_\star)^{-1}$. Beside the schematic response, which measures the *power* in the focal spot, integrated over the detected energy band, another possible description uses the intensity distribution. Since the spatial resolution follows the photon energy E linearly, the intensity is expected to increase with E^2 within the achromatic bandwidth. A zoomed representation of that focal intensity distribution for stepped hybrid

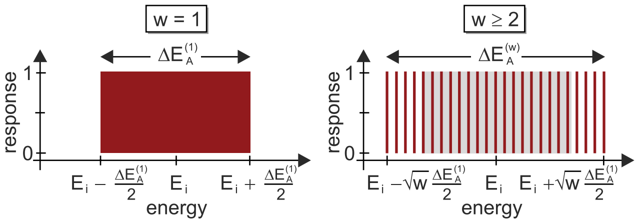

Fig. 9 Schematic representation of the spectral response in the focal plane around a central energy E_i with $4 \leq i \leq 8$ for full segments ($w = 1$) on the left and stepped versions ($w \geq 2$) on the right (red bars). Here, the light gray region represents the unstepped band for $w = 1$.

lenses is shown in Fig. 10 for $w = 2$ and $w = 10$, respectively. The comb-like peak structure may be interpreted as a series of purely diffractive intensity distributions, but now resulting from Fresnel lenses with only $mN_\star/2$ zones. Their individual bandwidth δE_{peak}—diffraction-limited by the 80% Strehl ratio—leads to an approximate number #(peaks) of spikes, i.e.

$$\delta E_{\text{peak}} = \frac{2E}{mN_\star} \quad \text{and} \quad \#(\text{peaks}) \approx \frac{1}{2}\sqrt{\frac{mN_\star}{w}}. \tag{30}$$

The net bandwidth that can be used for diffraction-limited imaging, i.e., which contributes to the luminous power, is thus given as the product $\Delta E_{\text{eff}} = \delta E_{\text{peak}} \times \#(\text{peaks})$ from Eq. (30) for $w \geq 2$. In summary, the effective spectral band can be written as

$$\Delta E_{\text{eff}}^{(w)} = \gamma_w (wmN_\star)^{-1/2} E \quad \text{for } w \geq 1. \tag{31}$$

For massive segments ($w = 1$), we have $\gamma_1 = 2$, whereas stepped versions with $w \geq 2$ are characterized by $\gamma_w = 1$.

The luminous power of an arbitrary achromatic lens with $w \geq 1$ is found with Eqs. (25) and (31) as

$$\frac{A_{\text{eff}} \times \Delta E_{\text{eff}}^{(w)}}{\pi(R_{\max}^2 - R_{\min}^2)} = \langle \hat{P}(E) \rangle_{\Delta E_A^{(w)}} \frac{\gamma_w E}{\sqrt{wmN_\star}} \mathcal{T}_w(s). \tag{32}$$

4.2 *Achromatic Gain*

Moreover, for a common focal distance instrument, that luminous power is found to factorize in the focal length and an independent factor which allows for an elegant optimization of $A_{\text{eff}} \times \Delta E_{\text{eff}}^{(w)}$. With $T_N = N/N_\star$, $R_{\max}^2 = (mN/2)\lambda F$, $R_{\min} = aR_{\max}$ and $\lambda = hc/E$, we obtain

$$A_{\text{eff}} \times \Delta E = \frac{\pi}{2} hc \mathcal{G}_w(N_\star, N_0) T_N (1 - a^2) F, \tag{33}$$

where the Planck constant and the velocity of light are denoted by h and c, respectively. From now on, the sub- and superscripts in ΔE will be omitted for simplicity.

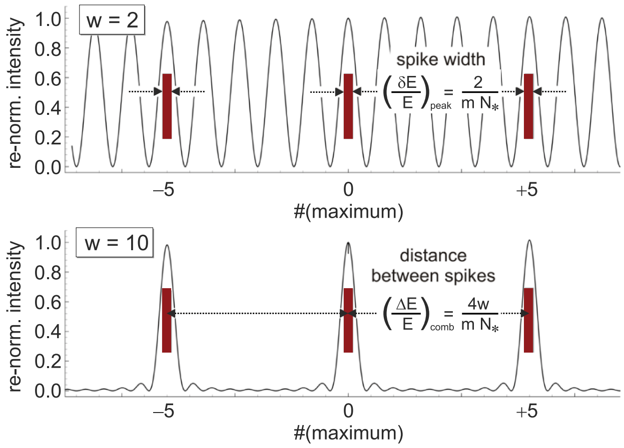

Fig. 10 Detailed structure of the focal peak intensity for the response from Fig. 9 for $w = 2$ and $w = 10$, numbered in units of positive and negative maxima. The zero-order spike is found at the central energy E_i. Dark red bars indicate the diffraction-limited spectral bandwidth $(\delta E/E)_{\text{peak}} = 2(\text{mN}_\star)^{-1}$ from the 80% Strehl ratio.

As initially introduced to describe the two-band prototype,[10] the "achromatic gain" $\mathcal{G}_w(N_\star, N_0)$ relates in its original definition the luminous power of an achromatic aperture to that of the sole diffractive component. Both differ from each other with respect to their transmission as well as bandwidth, and this gain may help to quantify the net effect of the technically laborious dispersion correction of a given Fresnel lens. In a more generalized version, the achromatic gain of an arbitrary segmented aperture now includes the Fresnel lens efficiency as well and is derived from Eqs. (32) and (33) to

$$\mathcal{G}_w(N_\star, N_0) \equiv \mathcal{W}_m^{(1)}(N_0)\gamma_w \left(\frac{m}{w} N_\star\right)^{1/2} \mathcal{T}_w(s). \tag{34}$$

The notation $\mathcal{W}_m^{(1)}(N_0) \approx \langle \hat{P}(E) \rangle_{\Delta E}$ indicates that this diffractive efficiency is independent from $N_\star$ up to its first expansion order with respect to the bandwidth, and in this approximation only determined by the absorption in the Fresnel component, following Eq. (5). By means of a partial differentiation $\partial_{N_\star} \mathcal{G}_w(N_\star, N_0) = 0$, the gain from Eq. (34) can be optimized with respect to an effective "hybrid zone number" $(mw^{-1})N_\star$ for a given N_0. The diffractive term $\mathcal{W}_m^{(1)}(N_0)$ does not affect the optimization; we obtain $(mw^{-1})N_\star \approx 2.51 N_0$ and the maximum amounts to

$$\mathcal{G}\text{opt}(N_\star, N_0) \approx 1.8 \mathcal{W}_m^{(1)}(N_0)\sqrt{N_0}. \tag{35}$$

The term $\mathcal{W}_m^{(1)}(N_0) \approx 1$ would reduce the gain by a few percentage at most for the monolithic optical systems as considered mainly in this work; it is hence neglected from now on in optimization-related issues. Figure 11 illustrates the achromatic gain under this assumption and the optimized zone number ratio in case of $w = 1$ for some values of N_0, typical for materials like Li or Be beyond ~5 keV. These lightest solid elements reach their maximum critical zone numbers of 1.2×10^3 (Li) and 8.0×10^2 (Be) beyond 10 keV. Approximated upper limits to the effective segment zone number $mN_\star$ are thus found as 3×10^3 and 2×10^3, respectively. In other words, the design of an achromatic system with maximized efficiency should not exceed $mN_\star \approx (2\text{–}3) \times 10^3$.

In Fig. 11, another modified definition of the gain is sketched in gray scale too, which incorporates the fact

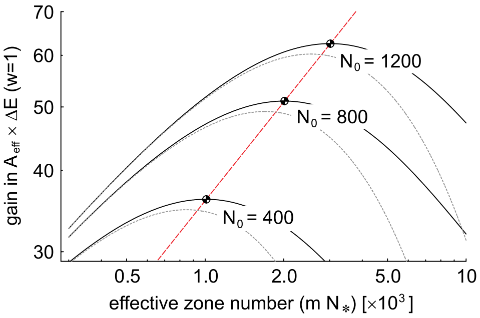

Fig. 11 Achromatic gain of segmented hybrid lenses with $w = 1$ for various N_0 parameters. The red dashed line refers to the optimized compensation with $(\text{mw}^{-1})N_\star \approx 2.51\, N_0$. The gray dashed curves include the degraded spatial resolution for $w = 1$ following Eq. (36), due to absorption.

that the nonuniform transmission through the lens segments leads to an enlarged focal spot size. Using the numerical results from Table 2, we define this corrected gain as

$$\mathcal{G}_{\varnothing}^{(1)}(N_\star, N_0) \equiv 2\mathcal{W}_m^{(1)}(N_0)\sqrt{mN_\star}\,\mathcal{T}_1(s)Q_1^{-2}(s), \tag{36}$$

where the squared dependence on $Q_1(s)$ accounts for the basic scaling law of all Fresnel-like optical systems: If the lens diameter is stretched by a certain factor χ while the zone number is kept constant, the focal spot size would also increase by χ. Accordingly, the focal length as well as the luminous power would be enhanced by χ^2. Under certain circumstances, especially where the focal spot size is crucial for the system design, the application of that slightly reduced gain (see Fig. 11) might be thus advisable.

4.3 *Weighted Gain for Stepped Segments*

Beside the strong absorption in segments with large s-ratios and $w = 1$, that degraded resolution is one of the reasons why coherent stepping is applied to hybrid lenses of that type. Following the arguments from above, the diffraction-limited detection of the spectral response of coherently stepped apertures decides on the optical efficiency with respect to the luminous power—together with the residual absorption, which is incorporated into the performance analysis like in the case of unstepped segments. We include both effects for such hybrid segments and generalize the corrected gain from Eq. (36) for $w \geq 1$, using Eq. (34) again:

$$\mathcal{G}_{\varnothing}^{(w)}(N_\star, N_0) \equiv \mathcal{G}_w(N_\star, N_0) \times Q_w^{-2}(s). \tag{37}$$

We may now relate this gain for an arbitrary reduction $w \geq 2$ to that for $w = 1$. Since the diffractive Fresnel lens is assumed to be the same, the quantity $\mathcal{V}_w(s)$ essentially compares the luminous power of the stepped and unstepped version with $w \geq 2$ and $w = 1$, respectively, weighted by the absorption-related PSF area. In

$$\mathcal{V}_w(s) \equiv \frac{\mathcal{G}_{\varnothing}^{(w)}}{\mathcal{G}_{\varnothing}^{(1)}} = \frac{\sqrt{w}}{2}\left(\frac{1-e^{-\frac{s}{2w}}}{1-e^{-\frac{s}{2}}}\right)\left(\frac{Q_1(s)}{Q_w(s)}\right)^2, \tag{38}$$

the transmission from Eq. (26) was used. The term $Q_1^2(s)Q_w^{-2}(s)$ accounts for the squared dependence of the luminous power on the focal spot size, i.e., $A_{\mathrm{eff}} \times \Delta E \propto \varnothing_{\mathrm{PSF}}^2 Q_w^{-2}(s)$ for a constant (total) zone number $N = T_N N_\star$. Figure 12 visualizes Eq. (38) for parameters $9 \leq s \leq 12$.

Obviously, unstepped segments ($w = 1$) are usually preferred, as long as $s \lesssim 8$. The focal spot correction is essential for this estimation: If the factor $Q_1^2(s)Q_w^{-2}(s)$ is omitted, the resulting "gain" would be limited to $\mathcal{V}_w(s) < 1$ even up to $s \approx 19$. Weighted for the spatial resolution, an optimized reduction follows the condition

$$w_{\mathrm{opt}} \approx [s/2] \quad \text{and} \quad \mathcal{V}_{\mathrm{opt}}(s) \approx c_0 \exp(c_1 s), \tag{39}$$

with $c_0 = 0.342$ and $c_1 = 0.132$ for approximated integers to $s/2$ and $s \geq 4$. For w, we find an exponential increase in the best stepping efficiency $\mathcal{V}_{\mathrm{opt}}(s)$. As expected, the reduction would again be most rewarding in case of low-transmission materials with large s-ratios; plastics like polycarbonate ($C_{16}H_{14}O_3$) with $N_0 \sim 10^2$ near 10 keV should be good candidates for strongly reduced optics with $w \gtrsim 5$. On the other hand, the usage of low-Z materials like Li in coherently stepped hybrid lenses is of interest only in case of large effective zone numbers ($mN_\star$). Near 12 keV for example, at least 10^4 Fresnel zones per segment are necessary for an efficient performance of such stepped lenses with $s \gtrsim 8$.

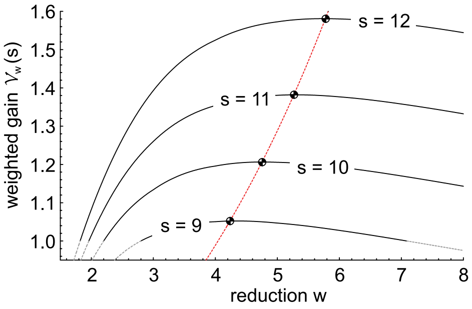

Fig. 12 Net "weighted gain" efficiency of coherent stepping for zone ratios $9 \leq mN_\star/N_0 \leq 12$ as a function of the saw-tooth number w. The optimized choice w_{opt} is indicated by the dashed red line and center-of-mass symbols.

Technical constraints would thus confine practical applications to lens materials with low N_0 rather than large zone numbers ($mN_\star$): As it follows from the local spectral bandwidth δE_{peak} in Eq. (30), high resolution imaging spectroscopes like transition edge sensors (TES) are to be employed, whose spectral selectivity will be limited. We appoint this circumstance in the next section.

5 Practical Design for Five Bands

The concepts from Secs. 2 to 4 are applied to the basic energy $E_0 = 40$ keV, corresponding to phase shift orders $4 \leq m_i \leq 8$ and an energy range 5 keV $\leq E_i \leq$ 10 keV. Beside astrophysical demands, i.e., the science case from Sec. 7, there are mainly two technical reasons for the choice of that spectral region: The quantum efficiencies of semi- and upcoming superconducting detectors are expected to maintain most of the focused flux up to $E_4 \approx 10$ keV, but not far beyond. On the other hand, soft x-rays of a few keV are strongly absorbed in all solid-state lens materials, which impedes an efficient achromatic telescope design.

5.1 *Selection of Suitable Materials*

Among them, pure lithium (Li) provides in principle an outstanding optical quality, i.e., an N_0 up to $\sim 10^3$. It may thus serve as a paradigm for the ultimate theoretical limit to the optical performance of such instruments. Due to its strongly corrosive behavior in air, machining and handling of compact amounts, i.e., lens segments, in a protective atmosphere would be clearly extremely challenging albeit not impossible. While the application of Li to practicable x-ray components is thus still in the fledgling stages,[16] Be has been widely used in the past for the fabrication of x-ray micro optics, especially compound refractive lenses (CRLs), and may be manufactured and handled without serious problems.[17] Its toxic dust—an inevitable waste product from mechanical processing—could be bound in oil, for instance. Despite its inferior critical zone number, elementary Be might serve as an alternative to Li. An extremely low content of foreign atoms is in any case of primary importance, since bulk and surface impurities will reduce the critical zone number at least for a contamination with heavy elements on a noticeable ppm level.[6] The extraction of ultra-pure materials, suitable for high-end x-ray optics, is not a trivial task. On the commercial level, almost perfect Li and Be samples with a purity up to 99.999% are nevertheless now available.[18,19] In this paper, we therefore assume the properties of idealized, pure Li and Be samples for the sake of simplicity, i.e., regardless of the current technological standard, and compare the performance of the lenses made from them. Afterward, the effect of "more realistic" lens materials with ppm impurities on the lens transmission will be briefly estimated.

5.2 *Optical and Technical Parameters*

As it will be discussed in more detail in Sec. 6, we assume in the following that an imaging spectroscope with a resolving power

$$(E/\Delta E)_{\mathrm{det}} \approx 2.5\times 10^3 \quad \text{for } 5\ \mathrm{keV} \le E \le 10\ \mathrm{keV} \tag{40}$$

serves as a detector. Such an instrument would permit the diffraction-limited (!) spike detection from coherently stepped ring lenses whose effective segment zone numbers $mN_\star$ may be twice as large, following Eq. (30) and in agreement with the chosen data from Tables 5 and 6 below. In other words, the zone numbers—in this case of nested apertures those of the outermost ring lenses—are chosen as large as the detector resolution would permit, to reduce the focal length.

On the other hand, the critical zone number of Li and Be ranges between 10^2 and 10^3, as listed in Table 7. We start with an (almost) optimized development of the Li-based optics, followed by an alternative design made of Be of similar or even identical geometrical dimensions.

Brief estimations show that zone numbers $N_\star \gtrsim 5\times 10^2$ are required—and allowed for stepped segments due to Eq. (49)—in the soft bands to keep the focal spot at an acceptable size of $\sim 10^{-3}$ m, in a distance of a few 10^2 km. Toward the hard x-ray bands, even larger zone numbers $\sim 10^3$ should be chosen, where the critical zone number nevertheless increases dramatically. Hence, the associated s-ratios $mN_\star/N_0$ exceed the critical lower limit $s_{\min} \approx 8.5$ for an efficient coherent reduction only in the two bands E_8 and E_7 for Li. Accordingly, the bands E_6 to E_4 should be designed for $w = 1$, since the critical zone numbers $N_0 \geq 7.5\times 10^2$ for $E \geq E_6$ are too large for an efficient coherent reduction as it was discussed in Sec. 4. Based on these facts, only the ring lenses for the "soft components" E_8 and E_7 (Li) will be stepped with $w \geq 2$, while an optimized luminous power in E_6 to E_4 is still obtained with massive segments.

Table 5 Optical and technical lens details (Li).

E_i	Energy	$\Delta\epsilon$	n_{FOV}	$N_\star$	R_i
E_8	5.0 keV	0.89 mas	230	600	1.80 m
E_7	5.7 keV	0.69 mas	295	704	1.44 m
E_6	6.7 keV	0.66 mas	311	800	1.15 m
E_5	8.0 keV	0.52 mas	395	1000	0.99 m
E_4	10 keV	0.43 mas	472	1200	0.84 m

Table 6 Optical and technical lens details (Be).

E_i	energy	$\Delta\epsilon$	n_{FOV}	$N_\star$	R_i
E_8	5.0 keV	0.89 mas	221	576	1.80 m
E_7	5.7 keV	0.65 mas	301	720	1.44 m
E_6	6.7 keV	0.73 mas	268	616	1.15 m
E_5	8.0 keV	0.85 mas	232	700	0.99 m
E_4	10 keV	0.61 mas	324	900	0.84 m

Within stepped or unstepped segments, the number of optically active, absorbing Fresnel zones is in any case effectively reduced to $(mN_\star)/w$. According to Eqs. (33) and (34), zone numbers $N_\star \sim (6{-}7)\times 10^2$ will nearly maximize the luminous power for a given focal length via $\mathcal{G}_w(N_\star, N_0)$ and an optimized reduction $w > 1$ due to Eq. (38). The data listed in Table 5 optimize $\mathcal{G}_w(N_\star, N_0)$ for E_8 ($w = 5$) and E_7 ($w = 4$) in the Li lens within an uncertainty of less than 1%. The overall and outermost lens radius $R = R_8 = 1.8$ m, obstructions $0.80 \leq a \leq 0.86$ and segment ring numbers $8 \leq T_N \leq 18$ are now adapted for the desired spatial resolution and the common detector size $r_{\mathrm{FOV}} = 15$ cm, which is moreover chosen here in all energy bands for the sake of simplicity. The HEW diameters range between $0.6\ \mathrm{mm} \leq \varnothing_{\mathrm{PSF}} \leq 1.3\ \mathrm{mm}$. The coherent reduction improves the spatial and angular resolution by about 26% in E_8 and 18% in E_7, compared to the unstepped analogue, while the transmission is enhanced from ~20% to 61% in both bands.

To maintain the comparability between the Li and Be version, the geometrical aperture data, i.e., the inner and outer radii of the ring lenses, are assumed to be the same. The design procedure turns out to be quite similar for Be. However, the increased absorption necessitates an extremely high degree of stepping up to $w_8 = 16$, now even in E_6 with $w_6 = 7$. In analogy to the Li version, the key data are summarized in Table 6. Obviously, the identical aperture and similar zone number data imply a comparable performance with respect to the resolution and the FOV, no matter which material (Li or Be) is used.

Table 7 Critical zone number data for Li and Be.

E_i	E_8	E_7	E_6	E_5	E_4
E [keV]	5.0	5.7	6.7	8.0	10
Li	442	575	753	967	1154
Be	140	185	255	363	527

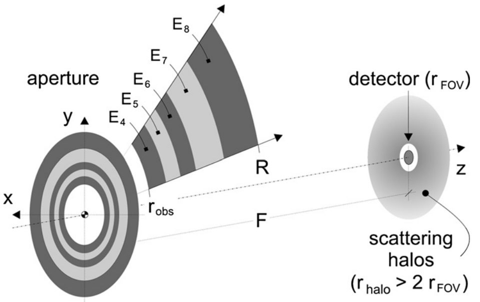

Fig. 13 Overall shape of the multiband telescope. Alternating gray levels in the aperture indicate various energy bands, as shown in the inset. The detector in the focal plane is surrounded by stray light halos. Dimensions are not to scale.

With an outermost minimum groove width of the Fresnel lenses between 0.9×10^{-4} m in E_4 and 1.7×10^{-4} m in E_8 both for Li and Be, the structuring procedure of the blazed Fresnel profile should be possible by means of molding (Li) or mechanical ruling (Be), rather than lithography (Sec. 5.4). This perspective is of particular interest for the proposed monolithic implementation, where the saw-tooth structure would be imprinted directly into the refractive prism shell (Fig. 7). Under these circumstances, an extra staircase sub-structure of the diffractive component, as it will be discussed in Sec. 5.5, might not be required any more.

The individual segments from which the aperture is composed (Fig. 6) measure $\gtrsim 5\times10^{-2}$ m. Despite their large number—in total, in the order of $\sim 10^3$ segments would have to be assembled—an economical strategy for their production should replicate efficiently the identical exemplars within each segment ring $k \le T_N$. While the lateral dimensions of the segments are the same for both materials, the aspect ratio $\mathcal{A}_i$ differs strongly: Defined as the ratio between height and lateral size of the prism-like refractive components, extremal values up to $\mathcal{A}_4 \lesssim 3$ are found for the Li version, whereas rather flat components with $\mathcal{A}_i < 1$ in all bands are possible in case of the relatively dense Be.

As it was shown in detail elsewhere,[6] the focal distance of segmented Fresnel x-ray telescopes is reduced in general by about one order of magnitude, compared to compact lenses. For the system parameters as assumed within this work, we obtain in particular

$$F_{\mathrm{Li}} = 302.5\ \mathrm{km} \quad \text{and} \quad F_{\mathrm{Be}} = 315.1\ \mathrm{km}. \tag{41}$$

The focal depth of field (DOF), determined from the wavelength λ and the numerical aperture (NA),[20] is enlarged by the number T_N of segment rings in each spectral band:

$$\Delta z_0 = \pm\frac{1}{2}\frac{\lambda}{(\mathrm{NA})^2}\times T_N \lesssim \pm 10^2\ \mathrm{m}, \tag{42}$$

This large focal depth clearly permits an uncritical axial detector position tolerance of several meters, as it will be picked up again in Sec. 6. An overall shape of the proposed telescope is sketched in Fig. 13. Here, the central obstruction of the whole aperture is denoted by $r_{\mathrm{obs}} = 6.7\times10^{-1}$ m. Unlike the sketched open hole in Fig. 13, the center of a real aperture should be filled instead, to protect the detector from direct zero-order illumination.

5.3 *Enhanced Performance in the Hard Bands*

The zone numbers $N_\star$ and other lens parameters for the hard bands around E_6 to E_4 in Table 5 or E_5 to E_4 in Table 6 have been adjusted for an angular or spatial resolution of similar magnitude as in the soft, coherently stepped bands. The relatively large fields of view with several 10^2 resolution elements in diameter come at the expense of a diminished effective area and bandwidth: With $N_\star \sim 10^3$, the criterion from Eq. (35) for a maximized luminous power in those bands is strongly violated—the corresponding s-ratios more or less exceed the optimum $s_{\mathrm{opt}} \approx 2.51$. However, the strict application of Eq. (35) would have implied an extraordinary large focal spot size of $(1\text{–}2)\times10^{-3}$ m in the Li version and even $(2\text{–}4)\times10^{-3}$ m for Be beyond 6 keV and 7 keV, respectively. Hence, for the design as summarized in Tables 5 and 6, somewhat larger values for $N_\star$ than suggested by Eq. (35) have been chosen.

Wherever this good spatial resolution is not of prime importance, the gain from Eq. (34) can be maximized to enhance the bandwidth-integrated effective area $A_{\mathrm{eff}}\times\Delta E$ on the price of smaller fields of view, compared to Tables 5 and 6. The results of this new priority are listed in Tables 8 and 9. For an angular resolution roughly twice as large as in Tables 5 and 6, a significantly enhanced luminous power can be achieved. In Fig. 14, the effective area and spectral bandwidth are illustrated as bar charts for both versions. The net collecting area of the mirror shells from Chandra and XMM-Newton exceeds or equals the Li or Be lens only in the soft bands, whereas the diffractive–refractive transmission optics are clearly favored toward the hard x-ray range.

Obviously, the "enhanced-throughput" version from Tables 8 and 9 benefits especially from an enlarged effective area, whereas the spectral bandpass is only slightly widened. This phenomenon can be understood from the strong impact of the geometrical zone number $N_\star$ on the lens transmission rather than on the bandwidth. Summed over all five bands, the luminous power of the Li version amounts to

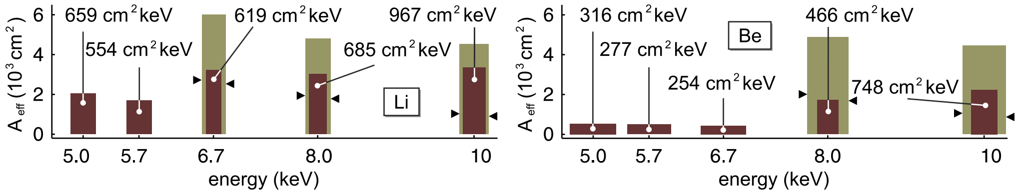

Fig. 14 Effective area and bandwidth for the Li (left) and Be (right) version in the monolithic implementation (see text). The data correspond to the configuration from Tables 5 and 6 (brown). Green columns represent the design according to Tables 8 and 9 for the unstepped ($w = 1$) segments. The bar width measures the spectral band $\Delta E_A^{(w)}$. For comparison, the net effective area of the mirror shells from XMM-Newton is indicated (arrow brackets ▶◀).

Table 8 High-throughput hard band features (Li).

E_i	$\Delta\epsilon$	n_{FOV}	$N_\star$	$A_{\mathrm{eff}} \times \Delta E$
E_6	1.49 mas	137	316	1838 cm^2 keV
E_5	1.00 mas	205	486	1556 cm^2 keV
E_4	0.69 mas	295	724	1682 cm^2 keV

Table 9 High-throughput hard band features (Be).

E_i	$\Delta\epsilon$	n_{FOV}	$N_\star$	$A_{\mathrm{eff}} \times \Delta E$
E_5	2.56 mas	77	182	2586 cm^2 keV
E_4	1.45 mas	135	332	2452 cm^2 keV

$$\sum_{i=1}^{5} A_{\mathrm{eff}}^{(i)} \times \Delta E_{\mathrm{eff}}^{(i)} = \begin{pmatrix} 3.5 \times 10^3 \\ 6.3 \times 10^3 \end{pmatrix} \mathrm{cm}^2\,\mathrm{keV} \tag{43}$$

for the standard and enhanced-throughput design, respectively. This sensitivity is comparable to that of Chandra, for instance—without consideration of the background, which is likely more significant for the separated spacecraft telescope. In case of the Be version, especially the standard configuration (brown bars in Fig. 14) exhibits an inferior luminous power, compared to Li:

$$\sum_{i=1}^{5} A_{\mathrm{eff}}^{(i)} \times \Delta E_{\mathrm{eff}}^{(i)} = \begin{pmatrix} 2.1 \times 10^3 \\ 5.9 \times 10^3 \end{pmatrix} \mathrm{cm}^2\,\mathrm{keV}. \tag{44}$$

5.4 *Li and Be in the Monolithic Scheme*

The calculations from above reveal that the monolithic lens design, which combines the diffractive and refractive components in a natural way, is regarded as the favored choice for an optimal performance near the theoretical limit. As it will be shown below in Sec. 5.5, an exceptional reproduction of the blazed Fresnel profile shape, rather than a too coarse multilevel approach, is of crucial relevance in the concept as considered here, using higher phase shift orders. Whereas almost perfect Fresnel lenses with a continuous profile function made of plastics such as PMMA are commercialized for the visible wavelength range, micro-structured low-Z x-ray optics of that kind are not available so far. E. M. Dufresne et al.[21,22] have made an "alligator" lens from Li, consisting of subsequent prism-like "teeth" with a minimum structure size down to ≈150 μm. Despite its geometrical simplicity, this row of micro-prisms might show the way to a successful molding of the Fresnel grooves in future, which are in fact of similar dimension (Table 10). Related to the constant profile depth of 517 μm for Li and 145 μm for Be, diffractive aspect ratios up to 2.90 (Li) and 0.78 (Be) must be realized in the splitted scheme with two symmetric saw-tooth profiles, one of them on each refractive half-shell (Fig. 7). With a

Table 10 Minimum Fresnel pitch for Li and Be.

E_i	E_8	E_7	E_6	E_5	E_4
Li lens	167 μm	160 μm	146 μm	118 μm	89 μm
Be lens	174 μm	166 μm	153 μm	123 μm	93 μm

Mohs hardness of only 0.6, Li is malleable, and one major challenge in fabrication concerns the careful retraction from the mold. Another open question is the durability, even under vacuum conditions. The alligator lens kept its quality for at least one year[21,22] and dedicated long-term tests over the projected mission lifetime of several years are without doubt required to judge the chemical and mechanical stability of Li micro-structures. Figure 15 illustrates a cross-section through the outermost Fresnel grooves. As opposed to Li, Be is well established as an x-ray lens material. Conventional engineering techniques are nevertheless difficult to apply,[23] and sophisticated structures are routinely formed instead by means of "Hot Isostatic Pressing" (HIP).[24] That technological access is facilitated by the strongly relaxed aspect ratios for the Fresnel lens compared to Li, as shown in Fig. 15. Meter-scaled, lightweight mirrors made of Be have been approved for the James Webb Space Telescope (JWST),[25] scheduled for launch in 2018. From today's point of view, this future space-based application probably confirms best the expected practicability of Be for diffractive x-ray optics of similar dimensions. Its high stiffness and excellent suitability for low-temperature, even cryogenic applications,[23] mark it as the likely material of choice for the realization of a mid-term mission for energies beyond about 4.5 keV.[7]

5.5 *Effects of an Imperfect Lens Design*

The calculations from above are based on the assumption of perfect optical components. In particular, the refractive lens materials Li and Be contain no foreign atoms, coatings, struts, etc., which all degrade the transmission. Moreover, the efficiency of the monolithic, encapsulated diffractive Fresnel lens reaches its maximum of almost 100% at the "lower harmonics" E_i, according to Eq. (9) and Fig. 2. In the following, both aspects are considered now for an imperfect, "real" lens design.

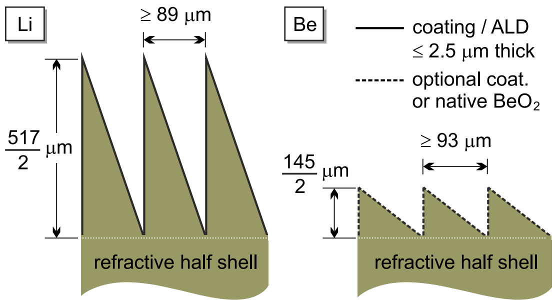

Fig. 15 Schematic view of the outermost, finest pitch for the monolithic Li and Be Fresnel components in true-to-scale dimensions. Refractive half shells are only shown in part. The coating will be discussed in Sec. 5.5.

- **Impurity analysis of Li and Be.** For a compound material with a homogeneous distribution of the atoms, the critical zone number is obviously obtained from a linear combination of the real and imaginary parts of the refractive index,[6]

$$N_0(E) = \frac{\sum_j \hat{w}_j \delta_j(E)}{2\pi \sum_j \hat{w}_j \beta_j(E)} \quad \text{with } 0 \leq \hat{w}_j \leq 1. \tag{45}$$

  The stoichiometric weight $\hat{w}_j$ accounts for the relative number of atoms from an element with index j within the unit volume. For impurities, this weight is very small ($\hat{w}_j \lll 1$) compared to the dominant material. Nevertheless, their pretended negligible amount—often in the order of several ppm—is largely overcompensated in the case of heavy elements by the strong dependence of the absorption on the atomic order number, $\beta_j \propto Z_j^3$. Trace amounts of metals like Fe, Co, or Ni, often incorporated during the production process, are thus particularly "dangerous," the more so as their K absorption edges of those and neighbored elements are located within the spectral range of interest. In contrast to their dramatic impact on absorption, atom-sized impurities are not suspected to cause significant stray light contributions to the background in the image plane, i.e., the scattering can be neglected. In fact, an analysis of commercially available Li and Be samples[10] revealed that trace impurities would change the imaginary part of the complex atomic scattering factor about two orders of magnitude more effectively than its real part. For an estimation of the expected loss, an averaged critical zone number $N_0^{(\text{real})} \approx 0.8 N_0^{(\text{pure})}$ with respect to the ideal maximum can be assumed, based on the numerical calculations for a Li sample of 99.99% purity.[6] Albeit costly, such an optical grade would be certainly available from current technology in the required amount. If all other design parameters are kept constant, an only moderate reduction of the optical performance by about 10% to 15% in $A_{\text{eff}} \times \Delta E$ is found.
- **Protective coating of Li.** The highly reactive alkali metal must not be exposed to its environment, not at all on earth for fabrication, but preferably also not during operation in space. One promising perspective to stabilize the Li surface might arise from the emerging field of atomic layer deposition (ALD), which allows for the deposition of nm-thin, tightly bonded films from various materials. More conventionally, an ultra-thin coating made of e.g. Teflon™ (C_2F_4) or Parylene-N™ (C_8H_8) should fulfill this requirement. The absorption length of those materials of $\sim 10^2$ to 10^3 μm would permit the fabrication of nonpermeable membranes with an inert behavior with respect to Li and—if necessary—Be. In view of chemical reactions with the lens surface to be coated, oxygen-containing materials like polymers need to be investigated carefully, however. For an assumed coating thickness of 2.5 μm, the four-fold (front and back side) Teflon™ layer would transmit 89% to 99%, depending on the energy. Using Parylene-N™, at least 98% could even be maintained.
- **Struts and support structure.** The listed data from Tables 5 to 9 and from Fig. 14 presume an idealized aperture, completely filled with the diffractive–refractive medium Li or Be. Though it greatly simplifies the calculations and provides the optimum in angular or spatial resolution as well as sensitivity, that picture does not recognize the degradation caused by struts and annular grid structures between individual segments. Furthermore, an additional internal "lattice" might be required,[6] since the fabrication of large blocks of Li or Be is not straightforward so far. Since space-based missions of that type have not been realized so far, an initial estimation is naturally difficult. As a rule of thumb, the mechanical framework might degrade the effective area of real telescopes by ~10% to 20%.
- **Fresnel lens fabrication from plastics.** The proposed embedded monolithic implementation of the Fresnel lens, directly milled at one half each into the two half shells of the refractive prisms-like segments, surely represents the most elegant solution. This option makes extremely high but not impossible demands on engineering skills for the sophisticated materials Li and Be. Wherever a more established technology is favored, separate Fresnel lenses made of plastics like polycarbonate ($C_{16}H_{14}O_3$) may be fabricated and attached to the Li or Be components. Such a heterogeneous approach implies an additional support layer for the saw-tooth Fresnel profile, associated with increased absorption. To stabilize the deep grooves of the continuous blaze profile over one whole segment size—the required $2\pi m_i$-thickness amounts to almost 200 μm —an underlying substrate of at least 50 μm is likely to be used. The diffraction efficiency of this device would decrease from 95% at 10 keV to 67% around 5 keV—even if an ideal Fresnel profile shape is assumed. Within the multiband scheme with its already modest efficiency in the soft bands (Fig. 14), an extra Fresnel lens made of plastics or an even worse material like Si is therefore not the very first choice, whereas the separated concept is certainly of great interest for other configurations that are used in their 1st phase shift order.[7]
- **Multilevel profile approximation.** An exact reproduction of the blazed, stepwise parabolic Fresnel saw-tooth profile is difficult in general, so a common approach often approximates the continuous profile function by several discrete steps, to obtain a staircase shape. However, that continuous Fresnel shape will be indispensable in fact for an at least near-optimal performance: Following a previous analysis of staircase profiles and their optical properties,[5] the diffraction efficiency is given as

$$\hat{P}_{m_i}^{(\mathcal{L})}(E_i) = \mathcal{G}_{m_i}^{(\mathcal{L})}(E_i)[\sin(\pi \mathcal{L}^{-1} m_i)/(m_i \pi)]^2, \tag{46}$$

  if used in its m_i'th order, with the absorption-related term

$$\mathcal{G}_{m_i}^{(\mathcal{L})}(E_i) \equiv \left(1 - e^{-\frac{m_i}{\mathcal{L} N_0}}\right)^{-2} \left(1 - e^{-\frac{m_i}{N_0}}\right)^2. \tag{47}$$

  The value of N_0 needs to be taken at E_i again. Applied to the multiorder concept used within this work, even

$\mathcal{L} = 10$ levels within one period would lead to a dramatic break-down in efficiency: No matter which material (Li or Be) is chosen for the monolithic implementation of the diffractive component, efficiencies between $\hat{P}_4(1/4) = 57\%$ and $\hat{P}_8(1/8) = 5\%$ are found. Similar results, only $\lesssim 2\%$ less, are obtained for the supported polycarbonate version from above, now with $\mathcal{L} = 10$ again. The general behavior of the diffraction efficiency as a function of the staircase number $\mathcal{L}$ is shown in Fig. 16. In the range below $\mathcal{L} \lesssim 10$, the higher-order efficiency falls down to a few percent or less, followed by the lower orders, e.g. E_4 for $\mathcal{L} \lesssim 5$. At certain values $\mathcal{L} \le 8$, the staircase profile even eliminates the efficiency in the corresponding phase shift order, i.e., where $\hat{P}_{m_i}^{(\mathcal{L})} < 10^{-3}$ in Fig. 16.

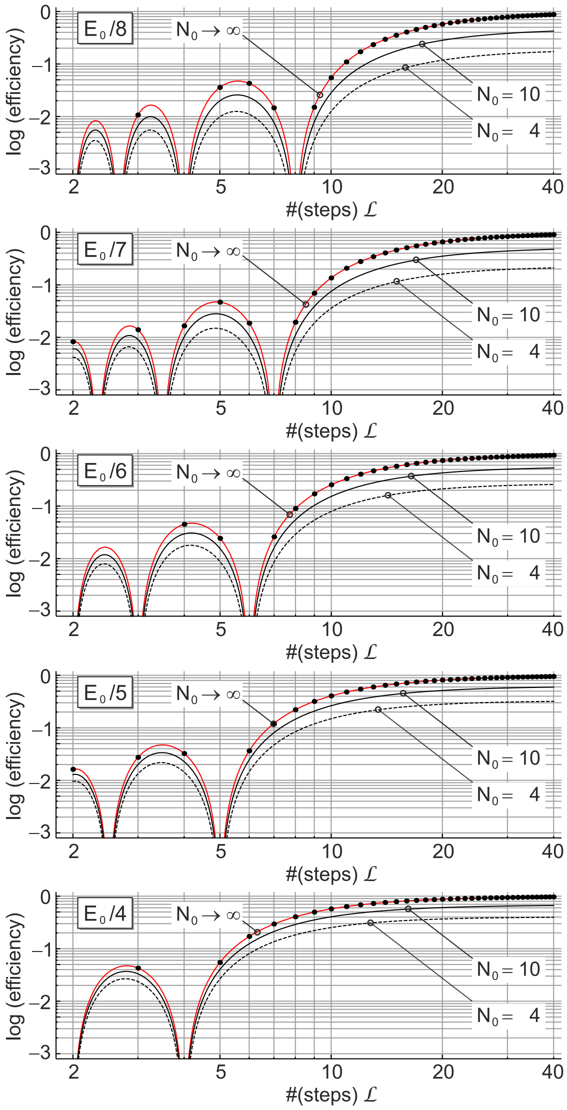

Fig. 16 Diffraction efficiency of a multilevel diffractive lens for $2 \le \mathscr{L} \le 40$ steps. For the lossless limit ($N_0 \to \infty$), discrete data (black dots) for all orders $E_8 \le E \le E_4$ are plotted together with the continuous function (solid red). Li and Be versions perform close to that limit. For illustration purposes, the strong absorption case with $N_0 = 10$ (solid black) and $N_0 = 4$ (dashed black) is also shown.

The continuous profile should be divided into 20, better 40 steps at least, to approach the high-performance limit of an ideal Fresnel lens. Regarding the smallest groove widths of $(0.9-1.7) \times 10^{-4}$ m from above, each step would need to be a few 10^{-6} m in width—an accessible regime for current micro-structuring techniques like photo- or electron-beam lithography and etchable Fresnel lens materials (for Li and Be, appropriate etching techniques are not obvious and still need to be developed).

This remarkable result proves that an almost ideal blaze profile is of crucial importance for the successful multiorder operation of x-ray Fresnel lenses and can be understood from the severe wave front perturbation caused by a too coarse staircase approximation. This disturbance becomes more and more significant the larger the phase shift within one groove will be, i.e., toward higher orders. From that point of view, the diffractive multilevel approach would mark the unique showstopper of all constructive imperfections as discussed so far, if less than ≈20 to 40 staircase levels are in use.

In summary, the overall expected loss in a real lens design may be estimated to about 30% to 40%, if only the first three influencing factors (material impurities, coating, and struts) from above are taken into account. That is, an almost perfect Fresnel lens is assumed, both in its shape—without or at least with an extremely fine staircase approximation—and implemented as a monolithic Li or Be version. In this case, the available total luminous power from Eqs. (43) and (44) is found as

$$(A_{\mathrm{eff}} \times \Delta E)_{\mathrm{real}} \gtrsim (1-2) \times 10^3\ \mathrm{cm}^2\,\mathrm{keV} \tag{48}$$

for the standard version (Tables 5 and 6) made of Li and Be, respectively. Despite this severe degradation, the residual sensitivity should be still sufficient if the observation time is correspondingly increased (Sec. 7). On the other hand, an inferior, badly structured diffractive plastic lens would downgrade the performance even more and should therefore be avoided in this special lens design, where the multiorder properties play the central role.

6 Focal Plane

The longitudinal range of permitted detector positions is limited by the focal depth of field, which is in the order of $\pm 10^2$ m for the focal distance of ~300 km, according to Eq. (42). Unlike those axial tolerances, denoted with "Δz" in Fig. 17, the uncertainty of lateral displacements $(\Delta x, \Delta y)$ of the detector spacecraft with respect to the optical axis is restricted to a few 10^{-4} m, i.e., an accurate lateral positioning well below the focal spot size is required for the detector spacecraft. Since the sensitive area is surrounded by extended stray light halos according to Fig. 4, the absolute position should be fixed at least within a few 10^{-3} m. The axial torsion may be roughly estimated to $\phi_z \approx \pm(2-4)$ arcmin for the outermost resolution elements on the circular detector plate of the Li and Be version, respectively.[6] In contrast, the "pitch and yaw" distortion angles α_x and α_y are less critical; and the corresponding errors scale with $1/\cos(\alpha_i)$. Despite initial studies,[26] the practical implementation of a precisely controlled formation flight system is still an

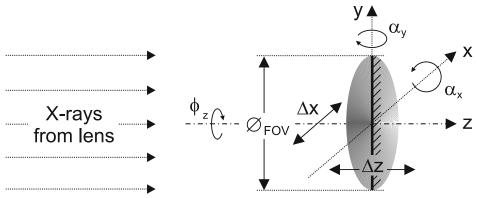

Fig. 17 Geometry of the detector unit and its degrees of freedom. Translational displacements are denoted by Δx and Δz; torsional tolerances are given as α_i and ϕ_z around the corresponding axes. The (circular) FOV is described by $\varnothing_{\mathrm{FOV}}$.

open question. Potential and promising technologies include triangle-like configurations with auxiliary satellites, as it is planned for the NGO mission (New Gravitational wave Observatory or "eLISA"), and the usage of next-generation compact x-ray lasers with low beam divergence. However, such issues are outside the scope of this work, and a perfect alignment is assumed in the following.

For the assumed detector diameter of 30 cm, the central fields of view cover almost 10^3 cm^2. Currently available, highly sensitive x-ray CCDs may be fabricated in that size.[27] As it was shown previously,[6] their energy resolution is well matched to the typical achromatic bandwidth of a few 10^2 eV for the hybrid lens in use; the diffraction-limited detection of the "hard bands" E_6 to E_4 for Li and E_5 to E_4 for Be is therefore definitely feasible with today's established technology. In Fig. 18, the peak intensity, relative to the incident radiation, is shown for both versions made of Li and Be in the energy bands E_8 to E_4. The scalar, paraxial diffraction integral was used to plot the functions shown in Fig. 18. It should be noted that, in order to obtain an optimal accuracy, the diffractive contribution as described in Eqs. (2) or (3) is included now for an assumed monolithic lens design and ideally shaped Fresnel grooves. Obviously, the hard bands show an almost constant but modest peak intensity over $\sim(2\text{–}6)\times 10^2$ eV, depending on the configuration (Tables 5 to 9).

6.1 *Remarks on Comb Detection*

In contrast, the large peak values up to $\sim 10^6$ for the stepped ring lenses in the soft x-ray bands (E_8 to E_7 for Li and E_8 to E_6 for Be) can be explained by the relatively high transmission, compared to the hard band components with massive segments. An efficient spectral discrimination of the spikes with an energy-resolving power $(E/\Delta E)_{\mathrm{det}} \approx 2.5\times 10^3$ in agreement with Eq. (30) and the data from Tables 5 and 6 is crucial for a diffraction-limited detection with an angular resolution close to the predicted milli-arcsec scale.

The defocused intermediate energies in between the spikes would in fact degrade the angular resolution, if they are not rejected by the energy-resolving detector. As it can be shown in a detailed analysis of the electromagnetic field distribution, an integration over the comb-like response with an ordinary CCD, for instance, would effectively degrade the spatial and angular resolution to a moderate multiple of the diffraction limit, i.e., to $\lesssim 10^{-2}$ arcsec. The exact factor by which the spot size would be enlarged depends on the distance between the spikes $(\Delta E/E)_{\mathrm{comb}} = 4w(mN_\star)^{-1}$ from Fig. 10 as well as on the response function of the detector itself. Clearly, strongly stepped optics ($w \gg 1$) approach the pure diffractive lens for $w \to N_\star/2$. In this limit, the dispersion correction would be completely lost and an achromatic bandwidth cannot be identified any more. The spatial resolution is thus expected to degrade, approximately proportional to the energy resolution ΔE_{det} of the detector. In the opposite extremal case, i.e., for minimal stepping with $w = 2$, the peaks are closely spaced (see Fig. 10), and an inferior detector resolution would only influence the spatial resolution in a minor extent. Moreover, a Lorentzian response function implies an even stronger degradation of the spatial resolution than a Gaussian response of the same spectral full width at half maximum (FWHM), if convolved with the energy-dependent PSF on and in between the spikes. For an initial estimation, the detector FWHM may be assumed to be the same as the energy distance between the spikes, $(\Delta E/E)_{\mathrm{det}} \approx (\Delta E/E)_{\mathrm{comb}}$. Under those conditions, as a rule of thumb, the Lorentzian response leads to an integrated focal spot size up to 3.5 times as large, roughly twice as much as for the Gaussian response. With respect to our sample design configurations, this would correspond to an absolute energy resolution of 20 to 70 eV. That still relatively strict demand cannot be fulfilled by conventional CCDs whose resolution is fundamentally limited to about 100 to 160 eV between 5 and 10 keV, and the spot size is supposed to be enlarged even more if such a CCD is used to detect the comb-like response in the soft bands: The energy-dependent focal spots will be superposed with equal weights within the whole range $\Delta E_A^{(w)}$ from Eq. (28). While the focal spot is diffraction-limited to $\varnothing_{\mathrm{PSF}}^{\triangle}$ on the spikes, its HEW diameter is expected to increase or decrease roughly in proportion to the energy in the spectral regions in between. As it is confirmed by strictly calculated HEW diameters using the diffraction theory, the spot size $\varnothing_{\mathrm{PSF}}^{\mathrm{ci}}$ for coherent stepping is at its maximum about $2.5\,w$ as large as on the spikes, that is in relation to $\varnothing_{\mathrm{PSF}}^{\triangle}$. This maximum is reached just at the mean between two adjacent spikes. The equal weighting hence results in an approximated formula for the effective spatial resolution,

$$\varnothing_{\mathrm{PSF}}^{\mathrm{ci}}(w) \approx \frac{5}{4} w \varnothing_{\mathrm{PSF}}^{\triangle} \quad \text{for } w \geq 2. \tag{49}$$

Table 11 gives an overview of the estimated imaging characteristics for an energy-integrated comb structure, following Eq. (49). Though the angular resolution $\Delta\epsilon_{\mathrm{ci}}$ would deteriorate simultaneously with the spot diameter $\varnothing_{\mathrm{PSF}}^{\mathrm{ci}}$, the practical effect of an unresolved comb structure on this latter quantity is even more serious, since it shrinks down the available FOV —expressed as $n_{\mathrm{FOV}}^{\mathrm{ci}}$ again—to only a few tens of the spot size, in particular for the Be version with its high level of coherent stepping ($7 \leq w \leq 16$). In return, and this might be the most convincing argument for a temporary comb integration via CCDs during operation, the luminous power would be strongly enhanced, as it is shown in Table 11.

In any case, a comparable performance would be expected if the coherent stepping is replaced by ordinary, optically independent segments (Sec. 3), now with $w = 1$ and of a correspondingly reduced size. In view of an easy fabrication, this option is likely favored over complicated stepping wherever suitable detectors, i.e., TES or MMC arrays, are not yet available.

It should be noted that this coarse estimation did not recognize the blurry shape of the PSF in between the spikes at all: In spatially extended, low-signal images of

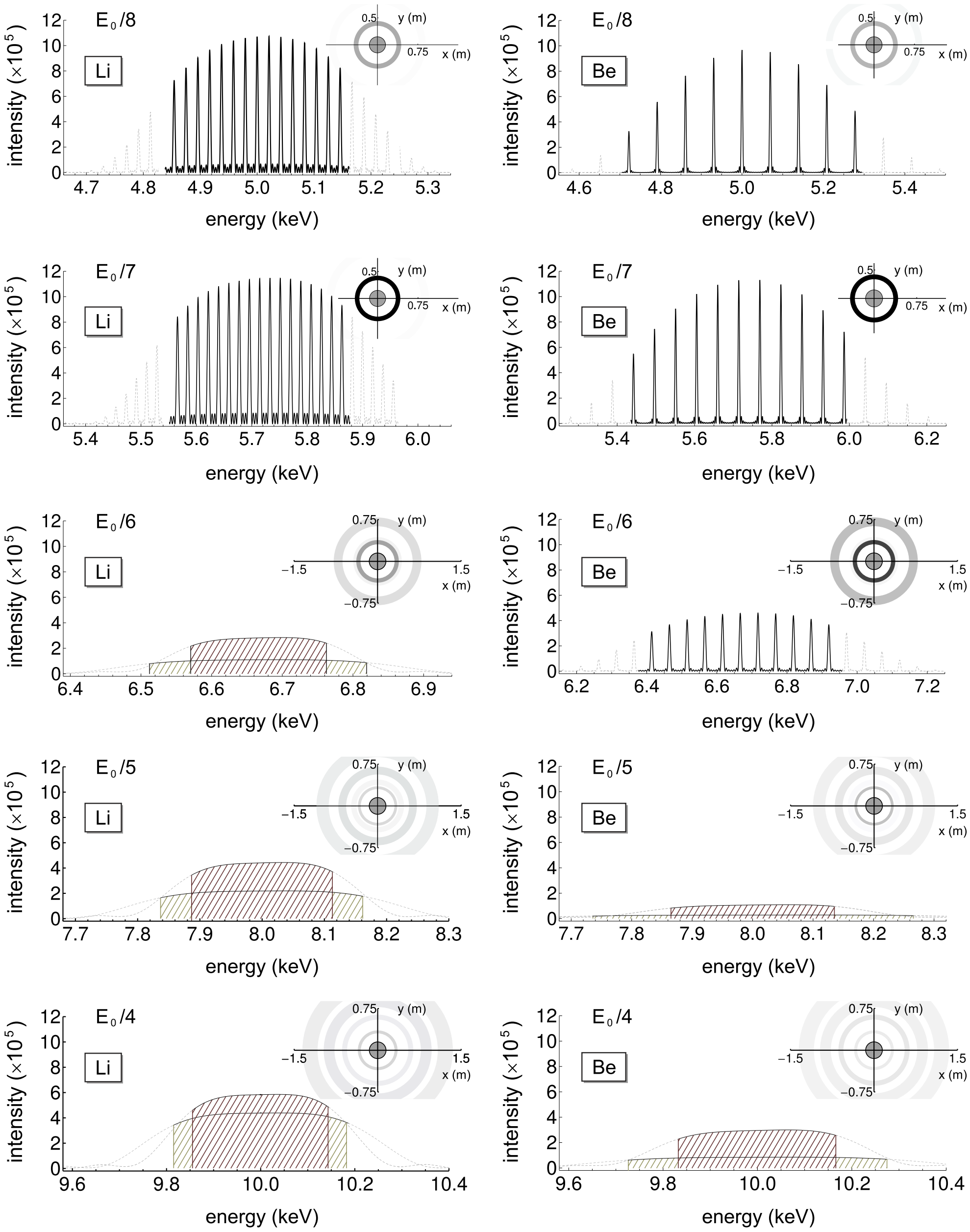

Fig. 18 Spectral response and scattering halos for the Li (left) and Be (right) version. The main images show the focal energy distributions; the black or hatched central sections indicate diffraction-limited detection. The insets illustrate the scattered halos around the circular detector. In the hard bands (E_4 to E_6 for Li and E_4 to E_5 for Be), the hatched color regions refer to the standard (brown) and "high-throughput" (green) design, respectively, from Tables 8 and 9. See text for details.

astronomical targets, the weak intensity of those defocused focal spots contributes effectively to the background level, reducing the achievable signal-to-noise ratio. However, these blurred focal spots exhibit regular patterns, characterized by an annular shape and an HEW diameter, which is a few times as large as that of the regular spot. Since their PSF is known and periodical in the energy, a potential deconvolution would be worthwhile to investigate, as long as the photon statistics are sufficiently good. An image reconstruction of that kind might help to enlarge the spectral band $\Delta E_{\mathrm{eff}}^{(w)}$ from Eq. (31) and thus the sensitivity for coherently stepped lenses with $w \geq 2$.

The issues as considered here reveal that there are in fact strong demands for a significantly improved spectral selectivity to resolve the comb structure, ideally near the diffraction limit according to Eq. (30). Hence, the desired resolving power of 2.5×10^3 corresponds to an absolute resolution of 2.0 to 2.7 eV in the soft energy bands. To date, superconducting TES achieve that goal indeed.[28] Micro-fabricated magnetic micro-calorimeters (MMC) might promise an even better performance; a possible resolution down to $\lesssim 1$ eV at medium x-ray energies has been predicted.[29] However, the realization of arrays of sufficient dimension, i.e., with a diameter of 30 cm, would be much more challenging than the fabrication of a CCD of the same size. Prototypes with 40×40 pixels are under development for ATHENA (formerly IXO), each pixel about $(300 \times 300)\,\mu\mathrm{m}^2$ in size.[30] Mega-pixel arrays similar to

Table 11 Performance for comb integration (CI).

Lithium	E_8 ($w_8 = 5$)	E_7 ($w_7 = 4$)	E_6 ($w_6 = 1$)
$\Delta\epsilon_{\mathrm{ci}}$ [arcsec]	6×10^{-3}	3×10^{-3}	—
$\varnothing^{\mathrm{ci}}_{\mathrm{PSF}}$ [m]	8×10^{-3}	5×10^{-3}	—
$n^{\mathrm{ci}}_{\mathrm{FOV}}$	≈40	≈60	—
$A_{\mathrm{eff}} \times \Delta E\vert_{\mathrm{ci}}$	6595 cm^2 keV	4435 cm^2 keV	—
Beryllium	E_8 ($w_8 = 16$)	E_7 ($w_7 = 12$)	E_6 ($w_6 = 7$)
$\Delta\epsilon_{\mathrm{ci}}$ [arcsec]	2×10^{-2}	1×10^{-2}	6×10^{-3}
$\varnothing^{\mathrm{ci}}_{\mathrm{PSF}}$ [m]	3×10^{-2}	1×10^{-2}	1×10^{-2}
$n^{\mathrm{ci}}_{\mathrm{FOV}}$	≈10	≈20	≈30
$A_{\mathrm{eff}} \times \Delta E\vert_{\mathrm{ci}}$	10106 cm^2 keV	6651 cm^2 keV	3558 cm^2 keV

CCDs with an unprecedented spectral sub-eV resolution are also considered for other future mirror-based x-ray missions, namely Generation-X.[31] As long as only small TES arrays are feasible, they could be alternatively integrated within large-scale CCDs for the hard spectral band—as a compromise to a fully exploited FOV in E_8 and E_7 (as well as E_6 for Be).

6.2 *Scattering Halos and Background*

In agreement with the rules from Sec. 2.2, the focal plane would be protected from any scattered radiation caused by stray light halos. For an on-axis point source, the defocused signal photons cross the focal plane within well-defined ring-like halos, whose inner diameter is at least twice as large as the detector plate. The dimensions of those soft and hard band stray light halos are compared to each other in the upper right insets of Fig. 18. In the general case including off-axis PSF distributions, the scattered stray light will be located within

$$r_{\mathrm{FOV}} \le r_{\mathrm{scat}} \le 3 r_{\mathrm{FOV}} + \Delta r_{\mathrm{halo}}, \tag{50}$$

where Δr_{halo} denotes the width of the annular stray light distribution. The scattered power—indicated by the gray level of the halo rings in Fig. 18—differs significantly for each band, due to different aperture radii and transmission. As it follows from Table 12, that luminous power equivalent exceeds the regular, focused x-ray light by one order of magnitude or more. We find that in the soft bands, the scattered power is mainly concentrated in only one, i.e., the innermost halo, created by the other coherently stepped ring lenses with their high transmission. Widely extended, meter-sized stray light distributions arise for the hard bands E_4 and E_5 (and also E_6 for Li).

Usually, the blurred photons in the halo region are lost for data acquisition. Nevertheless, the scattered flux might be collected and reconcentrated in the focal plane for "extra-sensitive" spectroscopy as long as the angular resolution—now degraded to ∼1 arcsec—is less important. In principle, custom-made capillary or micro-pore optics systems,[32] which cover the surrounding of the detector plate, are commercially available[33] and might be appropriate for this purpose. Such hollow-fiber bundles may have a typical transmission of ∼50% and can be tapered, to focus the x-rays to an additional energy-resolving but position-insensitive detector behind the main detector unit.

Table 12 Scattered power equivalent in halos.

E_i	E_8	E_7	E_6	E_5	E_4
E [keV]	5.0	5.7	6.7	8.0	10
Li ($\times 10^4$)	0.52	0.96	0.91	1.19	1.61
Be ($\times 10^4$)	0.81	1.64	2.44	1.52	2.06

7 Science Case

The instrument would have an angular resolution of about 10^{-3} arcsec, 500 times better than Chandra. Predictions on the scientific results of a "Fresnel mission," i.e., new objects or more detailed insights, are always speculative. Based on the current knowledge in x-ray astronomy, classes of targets can be identified however, with respect to their typical distance and dimension. Figure 19 illustrates for a couple of objects their approximated angular size. An angular resolution of 10^{-3} arcsec would provide access to the coronal emission from stars, orbits of x-ray binaries (XRB), far-distant supernova remnants (SNR) and the inner 0.1% in length of the jets from AGN, for instance.

The overall spectral width, which is covered by the multi-band telescope, amounts to more than 1 keV or 1/4 of the total range between 5 and 10 keV, as it is shown in Table 13. Hence, an application of the proposed achromatic instrument to broadband x-ray sources will be of particular interest, rather than to distinct sharp emission lines for which purely diffractive large-scale lenses would be more appropriate.[5] In particular, the energy conversion mechanism in the central

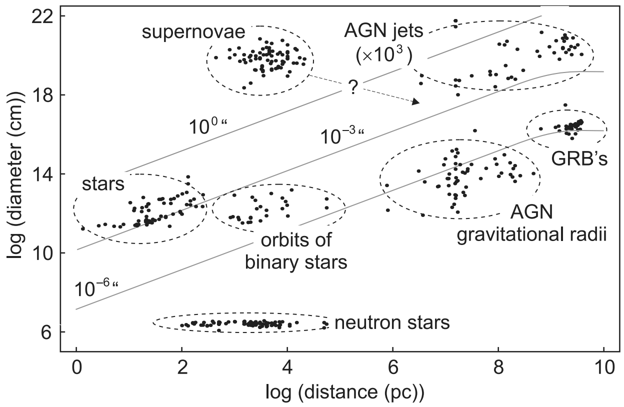

Fig. 19 x-ray targets on various distance and diameter scales. Examples of measured (stars, XRB, SNR, AGN) and partially simulated (NS, GRB) data are given.[34–40] Objects of the same class are grouped together (dashed lines).

Table 13 Total coverage within (5 to 10) keV.

Aperture version	Li	Li (hard)	Be	Be (hard)
Absolute bandwidth	1.4 keV	1.7 keV	2.3 keV	2.8 keV
Relative bandwidth	26%	31%	43%	50%

engine of an AGN provides a rewarding class of targets for future investigations.

7.1 *Observing the Central Engines of AGN*

In agreement with various existing unified models of AGN, the accretion disk is extended to 10^2 or even 10^3 gravitational "Schwarzschild" radii R_S, corresponding to typical angular diameters of 10^{-4} up to 10^{-3} arcsec. Similarly, though not yet confirmed so far, the jets are suspected to grow at a distance of $\sim 10^2\ R_S$ from the central mass.[41] Indicators have been found in observations for energy-dependent fluctuations in the x-ray luminosity, which are related to the disk-to-jet conversion mechanism.[41] The in- and outflows of matter are measured on a timescale of $10^6\ s$ or less. The luminosity of some famous nearby—and best resolved—AGN like Cen A, M 87 or NGC 4261 amounts to $\log L_x = (41 \pm 2)\ \mathrm{erg\,s^{-1}}$.

However, the even more distant BL Lac objects yield remarkable fluxes, too: The power law spectra of two examples, MS1229.2 + 6430 with a redshift $z = 0.164$ and H1426 + 428 ($z = 0.129$), are shown in Fig. 20. The signal counts compete with background contributions that originate mainly from distant AGN. Their averaged spectral emission up to 20 keV has been fitted[42] to

$$n_b(E) = n_0\ E^{-\Gamma} \quad \text{with } \Gamma = 1.42 \pm 0.02 \tag{51}$$

and $n_0 = (9.8 \pm 0.3)\ \mathrm{s^{-1}\,cm^{-2}\,keV^{-1}\,sr^{-1}}$. If the detection is geometrically collimated to an $f/10$-ratio, we have (thus with $\gamma = 10^{-1}$) a solid angle $\Omega \approx \pi\gamma^2$ the background is collected from. Within the five energy bands of the telescope, the mean contamination rates $\bar{n}_b$ range from $1.0\ \mathrm{cm^{-2}\,s^{-1}\,keV^{-1}}$ at 5 keV to $0.4\ \mathrm{cm^{-2}\,s^{-1}\,keV^{-1}}$ around 10 keV. We neglect any foreign background sources like cosmic rays, readout noise, etc. and estimate the signal-to-noise ratio (SNR) in each band:

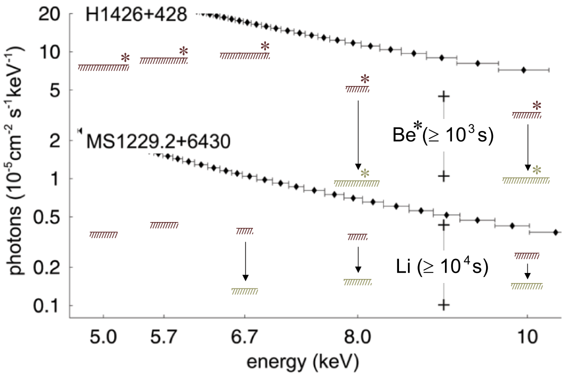

Fig. 20 Theoretical 5σ-limits to the point source continuum sensitivity for the standard (brown) and high-throughput (green) optics version for Li with an observation time of 10^4 s and Be (*,10^3 s), without fabrication losses ("≥"). The power-law spectra (black dots with error bars) represent XMM-Newton observations of BL Lac objects.

$$\frac{\mathrm{SNR}}{\sqrt{A\mathrm{eff} \times \Delta E}} \approx (\bar{n}_s \Delta t)^{1/2} [1 + \mathcal{F}_\Omega(\bar{n}_b)]^{-1/2}, \tag{52}$$

where $\bar{n}_s$ measures the mean signal counts in units of $\mathrm{cm^{-2}\ s^{-1}\,keV^{-1}}$ within an observation time Δt. Background corrections are introduced via

$$\mathcal{F}_\Omega(\bar{n}_b) \equiv \frac{\bar{n}_b}{\bar{n}_s} \frac{A_{\mathrm{PSF}}}{A\mathrm{eff}} \Omega, \qquad \text{with } A_{\mathrm{PSF}} \propto (\varnothing_{\mathrm{PSF}})^2, \tag{53}$$

as the focal spot area. Interestingly, the background term $\mathcal{F}_\Omega(\bar{n}_b) \ll 1$ from Eq. (53) reveals an almost signal- or photon-limited detection, for which we find the 5σ-sensitivity in the order of $5 \times 10^{-6}\ \mathrm{cm^{-2}\,s^{-1}\,keV^{-1}}$ or less for the Li standard version, if we assume an ideal optical instrument with the performance data from Sec. 5 and an exposure time of 10^4 s. The Be analogue still provides $\lesssim 1 \times 10^{-4}\ \mathrm{cm^{-2}\,s^{-1}\,keV^{-1}}$—but now for an observation time of only 10^3 s, for the sake of clarity in Fig. 20. These lower detection limits are also shown for the high-throughput version in the hard spectral bands (Tables 8 and 9) and compared to the blazar spectra. It should be noted that these limits rely on an idealized performance, according to Eqs. (43) and (44). Inevitable losses as described in Sec. 5.5 may be taken into account via an increased exposure time Δt, to maintain the sensitivity. Though also the relatively low noise level would increase with Δt, $\bar{n}_s \propto (\Delta t)^{-1}$ will hold approximately, according to Eq. (52). Hence, the observation time needs to be extended by about 40% to 70%, in agreement with the estimations from Sec. 5.5 and as summarized in Eq. (48).

7.2 *Targeting and Spacecraft Reorientation*

The long distance separation between the objective and detector spacecraft implies not only an extremely challenging—albeit feasible—formation flight, but also an enhanced time requirement for pointing at an x-ray source of interest. All extraterrestrial missions operated up to now consist of one sole and independent spacecraft, so there is a lack in practical experience. Formation flight systems are nevertheless under consideration for several forthcoming missions and, among others, Krizmanic et al.[26] have studied the projected operation of a similar Gamma-ray Fresnel telescope with a focal length of up to 10^6 km. Aside from this parameter, the expected time scale needed for reorientation is mainly determined by the averaged angular distance $\langle \Delta\vartheta \rangle_{\mathrm{target}}$ between prospective targets and the mean spacecraft velocity $\langle \Delta v \rangle_{\mathrm{RP}}$ when moving to a new position. Within the scaled-down pathfinder mission, Krizmanic et al. assume two weeks for that movement to another source in an angular distance of 20 deg, if the (detector) spacecraft in a focal distance of 10^5 km is relocated with a mean velocity of $120\ \mathrm{m\,s^{-1}}$. We reduce that repointing speed to a more relaxed velocity of $\approx 20\ \mathrm{m\,s^{-1}}$ as it was formerly proposed for the MAXIM pathfinder.[43] Together with the focal length from Eq. (41), we obtain

$$\langle \Delta\tau \rangle_{\mathrm{RP}} \approx 6\,\mathrm{h} \quad \text{for } \langle \Delta\vartheta \rangle_{\mathrm{target}} = 20\ \deg. \tag{54}$$

An even further reduction of that already short timescale is expected in the x-ray band of a few keV, since targets in this range are by far more frequent than Gamma-ray sources of sufficient brightness. As an example, the mean angular next neighbor distance between the 90 brightest stars with an apparent magnitude of 2.5 or less and presumed coronal x-ray emission can be simply estimated to ∼10 deg.[34,44] On the other hand, accreting central cores of far-distant galaxies, i.e., AGN, mainly constitute the x-ray background.[45] The surface density of those discrete sources was determined to $\sim 10^2$ deg^{-2} in this 21-year-old ROSAT study, which only resolved the brightest sources of that type back then. An universal, typical angular distance $\langle\Delta\tau\rangle_{\text{RP}}$ can therefore hardly be identified and the actual scale is determined from "what is wanted to be seen." In any case, the 20 deg mark with its ≈6 h reorientation time may be regarded as an upper limit for most maneuvers of that kind.

8 Conclusion

In summary, an efficient concept for the simultaneous imaging in multiple energy bands between 5 and 10 keV is developed for dispersion-corrected, high-resolution x-ray telescopes. The scheme is designed for a shortened focal length, as compared to former versions: The usage of higher phase shift orders of the Fresnel lens permits an efficient nesting of several annular apertures for closely spaced energy bands. The typical focal spot size around 10^{-3} m results in an angular resolution of about 10^{-3} arcsec throughout the whole spectral range. With an aperture diameter of 3.6 m for both suggested versions made of Li and Be, the total luminous power is estimated to at least $(1\text{–}2) \times 10^3$ cm^2 keV, respectively—even under realistic assumptions on potential technical imperfections. The associated sensitivity is comparable or superior to that of Chandra above ∼3 keV. Table 14 gives an overview of the most important parameters in the standard configuration from Tables 5 and 6. For the resolution $\Delta\epsilon$ and the number n_{FOV} of resolution elements across the detector plate diameter, standard errors indicate the variation over the five energy bands, whereas in case of the focal length, the ± range describes the smallest DOF. The 5σ-sensitivity is given in units of $[\text{cm}^{-2}\ \text{s}^{-1}\ \text{keV}^{-1}]$ for an observation time of 10^5 s in each case now and allows for an assumed loss due to technical imperfections in the range from 0% to 40%.

Table 14 Summary of the telescope performance.

Parameter	Li	Be
$\Delta\epsilon$	0.64 ± 0.18 mas	0.75 ± 0.12 mas
n_{FOV}	$341 \pm 94\, \varnothing_{\text{PSF}}$	$269 \pm 44\, \varnothing_{\text{PSF}}$
$F \pm \Delta z_0$	302.5 ± 60.5 km	315.1 ± 62.5 km
$(\Delta E)_{\text{total}}$	1.4 keV (26%)	2.3 keV (43%)
$\bar{n}_s[5\sigma]$	$(0.7\text{–}1.2) \times 10^{-7}$	$(1.2\text{–}2.0) \times 10^{-7}$

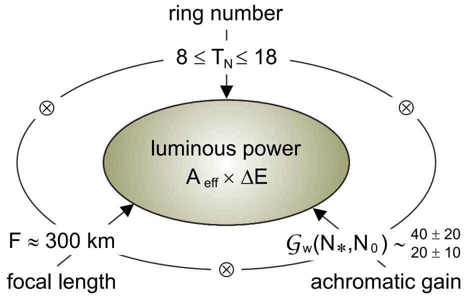

Fig. 21 The luminous power of multiband telescopes factorizes into the common focal length F, the number T_N of segment rings per energy band and their achromatic gain $\mathcal{G}$.

From a theoretical point of view, an analytical formalism is presented that may support in principle the development of arbitrary large-scale, nested apertures. The substantial complexity of this task in the case of achromatic imaging with minimized background contributions is tackled with flexible criteria for an optimized, high-throughput construction. In general, the geometrical parameters of diffractive focusing optics as well as the lateral and longitudinal dimensions in the focal region follow a scaling law—the luminous power but also the spot size would increase with the focal length and the aperture radius, if the zone number is kept constant. Vice versa, an adjusted zone number for a given lens material and the desired spatial resolution will maximize the sensitivity for the common focal length. The segmentation scheme as proposed in this and former work introduces another degree of freedom in the multispectral lens design—and greatly mitigates, by the way, the challenges in fabrication. In Fig. 21, a schematic illustration is given on how the segmented (ring) lens telescope attains its luminous power. According to Eq. (33), three factors—the number T_N of segment rings, the gain $\mathcal{G}_w(N_\star, N_0)$ and the focal length F—contribute in a multiplicative way to $A_{\text{eff}} \times \Delta E$. While the focal length is the same for all bands and differs only marginally from Li to Be, the variable quantities T_N and $\mathcal{G}_w(N_\star, N_0)$ mainly account for the energy-dependent sensitivity in our scheme. In Fig. 21, the gain is given for both versions and, interestingly, the Li version with $\mathcal{G}_w(N_\star, N_0) \sim 40 \pm 20$ (above) performs roughly twice as well as the Be lens (20 ± 10) with respect to this criterion. Since the mean segment ring number $\langle T_N \rangle_i$ is comparable for both versions, the higher sensitivity of the Li lens is only based on this material-dependent term and may be regarded as the strongest argument for the usage of Li.

The fundamental difference of such multiband apertures to single-band achromatic instruments[6] should be emphasized: Whereas lenses of the former type are constrained by the common focal distance and optimized for $N_{(\star)}/N_0 \to 2.51$, optics of the second kind are based on the "boundary condition" of a given focal spot size $\varnothing_{\text{PSF}}$ and yield their best performance for $N_{(\star)}/N_0 \sim 5$.

Ultra-pure Li or, alternatively, Be is preferably chosen for the monolithic diffractive–refractive lens components. Their optical properties are best used for a certain deflection power, expressed by an effective hybrid zone number. On the other hand, Li in particular is challenging to fabricate on the required level of accuracy[6] and would need at least some coating by an ultra-thin plastic foil or ALD for instance, to protect the reactive alkali metal from the environment.

There is little practical experience so far, except from prototype optics like elementary refractive lenses,[16] and serious experimental efforts will be necessary to exploit the outstanding optical potential of Li in future. Be will probably serve as the more practical alternative for short-term proof-of-concept "pathfinder" studies and also full-size missions.[7] Despite its worse transmission, the higher density and refractive power enables a more relaxed lens design in terms of the aspect ratio. Moreover, its greater hardness and stability compared to Li should ease the precise fabrication of the Fresnel grooves.

A plastics Fresnel lens has been shown to be of limited transmission in the soft bands in particular, not only as of the refractive $2\pi m_i$ phase shift thickness, but also due to the supporting layer, which was assumed to have a minimum thickness of 50 μm (Sec. 5.5). Nevertheless, its combination with refractive lens components made of Be likely marks the most attractive type of all hybrid optics as discussed so far under the criterion of technical feasibility. A similar approach was also proposed for the MASSIM mission,[7] and it might be worthwhile to investigate the performance of this heterogeneous implementation. For the data in the right column ("Be-PC") of Table 15, the Be Fresnel lens from the monolithic scheme (summarized in Table 14) is simply replaced by the polycarbonate device as described above. All other lens design parameters have been adopted from the monolithic version, and the worse 5σ-sensitivity $\bar{n}_s$ within 10^5 s is the only difference. Though the polycarbonate membrane absorbs primarily in the soft bands where the effective area is already low, the total loss is modest and suggests indeed the construction of an initial instrument with a plastics Fresnel lens inside. One could even think about a sole diffractive telescope, without any dispersion correction. If this diffractive lens is made again from polycarbonate, its net performance can be directly compared to the Be-PC configuration. Except from the grating period or "pitch," which is taken twice as large to achieve the same focal length, we maintain all other design parameters. The result is shown again in Table 15. As expected, the angular resolution $\Delta\epsilon$ is slightly better, since the full segment size now contributes to the diffraction pattern, without the gray wedge effect from the refractive component. The individual spectral width in each of the five bands follows Eq. (27) and amounts to 2 to 6 eV—no more than 18 eV in total. Together with the rather weak sensitivity—about one order of magnitude worse than for the Be-PC scheme—those narrow individual bandwidths make that sole diffractive version unattractive: High-end TES or MMC arrays that would detect just five relatively narrow bands up to 10 keV are likely not available and/or are ineffective in their use.

Table 15 Plastics Fresnel lens performance.

Parameter	Sole PC	Be-PC
$\Delta\epsilon$	0.68 ± 0.13 mas	0.75 ± 0.12 mas
n_{FOV}	$297 \pm 55\,\varnothing_{\mathrm{PSF}}$	$269 \pm 44\,\varnothing_{\mathrm{PSF}}$
$F \pm \Delta z_0$	315.1 ± 62.5 km	315.1 ± 62.5 km
$(\Delta E)_{\mathrm{total}}$	0.02 keV (0.4%)	2.3 keV (43%)
$\bar{n}_s[5\sigma]$	$(1.2–1.5) \times 10^{-6}$	$(1.4–2.3) \times 10^{-7}$

Apart from technological efforts to be made in accurate formation flying, the development of large TES or MMC arrays is essential for the successful performance at the diffraction limit. A spectral selectivity near 2.5×10^3 would result in an almost perfect image quality for x-rays of a few keV. Using currently available MMC arrays with a resolving power of $\approx 10^3$ instead would enlarge the spatial and angular resolution in the soft bands with coherent stepping by a modest multiple of the diffraction-limited optimum—together with an increased effective area, since more photons are collected now.

In further research steps, optimized optical arrangements with eventually even more closely spaced spectral bands might be identified. From an astrophysical point of view, angular resolution, multiple bandwidth detection, and good point source sensitivity of the optics as presented in this work should nevertheless already match the minimum requirements for fruitful observations of inner disk-jet regions of nearby and sufficiently bright AGN, recording fractions of their power law spectra, and determining their characteristic index.

Appendix A: Fresnel Lens Terminology

Within this work, the term "Fresnel lens" means a fully blazed diffractive profile, whereas a simple zone plate (ZP) is characterized by its binary thickness function. There are different notations in the literature, however. In the x-ray microscopy community, mainly binary amplitude zone plates with alternating open and opaque zones are in use, due to their simplicity in nano-fabrication. Their (± 1) st order efficiency is limited to ≈ 10%, however; and 30% of the incident light are diffracted into the 0th and higher orders. This poor imaging performance is acceptable in on-axis scanning applications with a sufficiently bright illuminating source, e.g. at synchrotron beamlines,[20] and only partially improved for more or less transparent phase zone plates.[46] A significant step toward an enhanced $(+1)$st order efficiency is made with multilevel (phase) zone plates, which consist of a staircase profile within each grating period.[47] The more steps ($\mathcal{L}$) the profile is divided in, the better the ideal blazed Fresnel structure will be approached and the $(+1)$st order will dominate more and more the diffraction characteristics.[5] In the limit of a Fresnel lens with $\mathcal{L} \to \infty$, the $(+1)$st order may reach an efficiency up to 100%, less absorption losses (see text). For one period, that constructive transition is sketched in Fig. 22.

It turns out that, due to the peculiar functional relation between the refractive index increment and the energy ($\delta \propto E^{-2}$), the Fresnel x-ray lens is blazed not only to one unique energy.[5,10] Instead, the conjunction of the continuous profile with the squared energy dependence of the refractive power leads to an additional occurrence of distinct "phase shift orders" for a discrete set of energies, for which an efficiency up to 100% would be found, less the absorption again. To avoid confusion, it should be noted that this special definition of the "phase shift order" m_i is distinct from the common "diffraction order" m as it is used in grating theory and

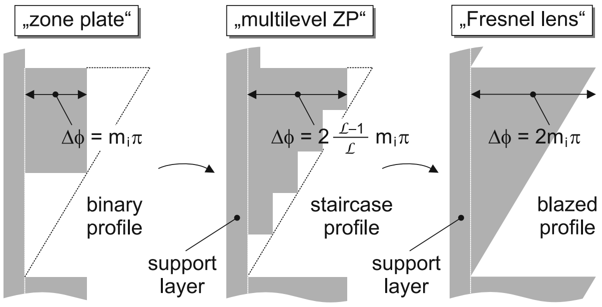

Fig. 22 From binary phase “zone plates” (left) to fully blazed “Fresnel lenses” (right) in the x-ray band. “Multilevel ZPs” with their staircase profile represent an intermediate version. The phase shift ranges between $m_i\pi \le \Delta\phi \le 2m_i\pi$.

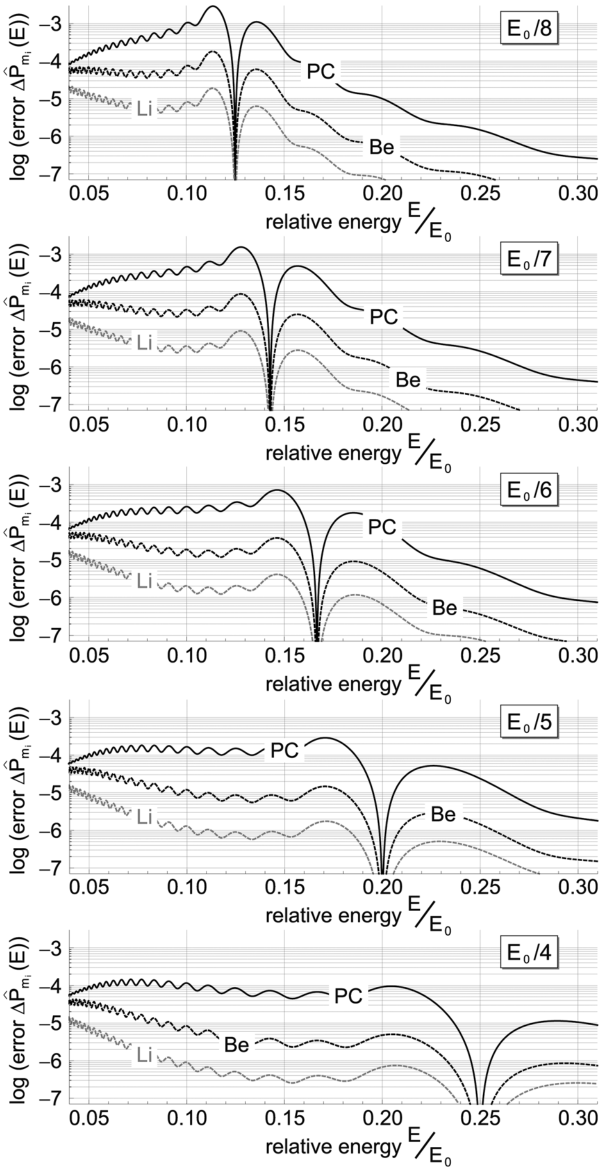

Fig. 23 Absolute difference (“error” $\Delta\hat{P}_{m_i}(E)$) between the diffraction efficiencies $\hat{P}_{m_i}(E)$ as obtained by the exact Eq. (2) and its approximation, Eq. (3). Results for Fresnel lenses made of polycarbonate (PC), Be and Li are shown.

described by the well-known grating equation for one single wavelength or energy. Hence, the energy-related subscript i with $i \ge 1$ is introduced to indicate that special subset within all possible orders into which the photons may be focused. Several authors investigated in the past optical systems similar to the one considered here. H. Dammann calculated the diffraction properties of blazed and staircase structures, including higher orders, for the visible wavelength range.[14] A roughly constant refractive index in this regime restricts in fact the useability to one unique spectral region and losses into others than the $(+1)$st order arise only from an imperfectly satisfied blaze condition, either due to a slightly mistuned wavelength or because of an approximated, i.e., staircase profile. With respect to partially absorbing binary x-ray phase zone plates, those ordinary diffraction orders were in particular analyzed by Kirz,[46] for instance. It is found that, in contrast to the visible regime, the inevitable absorption implies an additional source of diffraction into multiple orders, at the expense of a lowered $(+1)$st order net efficiency. In our analysis however, the phase shift order represents the main—and in the virtual case of no absorption—sole order into which the radiation is concentrated if the phase condition $\Delta\phi = 2m_i\pi$ (Fig. 2) for an integer $m_i \ge 1$ or—equivalently—the energy relation $E_i = m_i^{-1}E_0$ is fulfilled. Some small fractions of the incident radiation would be nevertheless diffracted into neighbored orders to m_i in the case of absorbing Fresnel grooves or if the phase condition is violated—see Eq. (3).

Appendix B: Factorization of Eq. (2)

For each integer $m_i \ge 1$ and sufficiently large critical zone numbers $N_0 \gtrsim 10$, Eq. (2) represents a “sinc-like” energy dependence around $E_i = m_i^{-1}E_0$ similar to Eq. (4), whose local maximal and minimal values are slightly modified by absorption. This fact motivates an approximative factorization of $\hat{P}_{m_i}(E)$, where the term $\mathcal{U}_{m_i}^{(Z)}(E)$ depends only implicitly on the energy via $N_0(E)$, determining the achievable efficiency in E_i. Both factors in Eq. (3) are found as limits of the full Eq. (2):

$$\lim_{E\to E_i}\hat{P}_{m_i}(E) = \mathcal{U}_{m_i}^{(Z)}(E_i) \tag{B1}$$

$$\lim_{N_0\to\infty}\hat{P}_{m_i}(E) = \hat{P}_{m_i}^{(0)}(E) \tag{B2}$$

The difference $\Delta\hat{P}_{m_i}(E)$ between Eqs. (2) and (3) is largest in the first minimum on the left and right of the main peak at the respective phase shift order, where only the factorized approximation yields $\hat{P}_{m_i}(E) \to 0$, regardless of N_0. Both expressions coincide, however, toward the spectral range of interest, i.e., $\lim_{E\to E_i}\Delta\hat{P}_{m_i}(E) = 0$. Figure 23 illustrates this numerical error for the Fresnel lens materials in use. Obviously, with $\Delta\hat{P}_{m_i}(E) \lesssim 10^{-4}$ near E_i, the deviations are in fact negligible and Eq. (3) is accurate enough in all calculations of practical interest.

Appendix C: Math Nomenclature

Table 16 Global symbols and geometrical optics.

Symbol	Description	Usage or (unit)
R	outer, total lens radius	$[R] = \mathrm{m}$
E	photon energy	$[E] = \mathrm{keV}$
F_Z	diffractive focal length	$F_z = R^2/N\lambda$
F_L	refractive focal length	$F_L = -2F_Z = -F$
F	common focal length	$[F] = \mathrm{m}$ or km
ζ	fractional focal distance	$\zeta \equiv z/F$
f	f-ratio or f-number	$f = F/2R$

Table 17 Multi-order Fresnel imaging.

Symbol	Description	Usage or (unit)
R_i	outer lens radius for E_i	$[R_i] = \mathrm{m}$
E_0	global reference energy	$[E_0] = \mathrm{keV}$
m_i	phase shift order for E_i	$m_i \geq 1, \; m_i \epsilon \mathbb{N}$
E_i	ring lens design energy	$E_i = E_0/m_i$
ψ_{ij}	relative energy	$\psi_{ij} \equiv E_j/E_i$
ζ_{ij}	fractional focal distance	$\zeta_{ij} \equiv (m_i/m_j)^2$

Table 18 Zone number related quantites.

Symbol	Description	Usage or (unit)
N	#(geom. Fresnel zones)	$R^2 = N\lambda F_Z$
N_0	critical zone number	$N_0 = \delta/(2\pi\beta)$
s	effective zone ratio	$s \equiv mN_\star/N_0$
$\Delta t_{2\pi}$	2π-(phase shift) thickness	$\Delta t_{2\pi} = \lambda/\delta(\lambda)$

Table 19 Parameters for segmentation.

Symbol	Description	Usage or (unit)
$N_\star$	#(Fresnel zones/segment)	$N_\star < N$
T_N	#(segment rings)	$T_N \equiv N/N_\star$
k	segment ring index	$1 \leq k \leq T_N$
r_k, φ_q	segment boundaries	$r_k \propto \sqrt{k}, \; \varphi_q \leq 2\pi$
a	central lens obstruction	$0 \leq a \leq 1$
$\eta_N(a)$	obstr. conversion factor	$\eta_N(a) \sim 3.0 \pm 0.6$

Table 20 Parameters for coherent stepping.

Symbol	Description	Usage or (unit)
w	#(coherent steps)	$N_\star(4w)^{-1}\epsilon\mathbb{N}$
$Q_w(s)$	abs.-degraded resolution	$Q_w(s) \gtrsim 1$
γ_w	comb detection factor	$\gamma_1 = 2; \; \gamma_{w\geq 2} = 1$
$\mathscr{G}_w$	achromatic gain	$\mathscr{G}_w = \mathscr{G}_w(N_\star, N_0)$
$\mathscr{G}_\varnothing^{(w)}$	PSF-corrected gain	$\mathscr{G}_\varnothing^{(w)} = Q_w^{-2}(s)\mathscr{G}_w$
$\mathscr{V}_w(s)$	weighted stepping gain	$\mathscr{V}_w = \mathscr{G}_\varnothing^{(w)}/\mathscr{G}_\varnothing^{(1)}$
δE_{peak}	comb peak bandwidth	$\delta E_{\mathrm{peak}} = 2E/mN_\star$

Table 21 Efficiency/luminous power calculation.

Symbol	Description	Usage or (unit)
$\hat{P}_{m_i}$	Fresnel lens efficiency	$\hat{P}_{m_i} \approx \mathscr{U}_{m_i}^{(Z)} \times \hat{P}_{m_i}^{(0)}$
$\mathscr{U}_{m_i}^{(Z)}$	Fresnel absorption factor	$\mathscr{U}_{m_i}^{(Z)}(E_i) \lessapprox 1$
$\hat{P}_{m_i}^{(0)}$	Fresnel diffraction factor	$\lim_{E\to E_i} \hat{P}_{m_i}^{(0)} = 1$
$\mathscr{T}_w(s)$	*refractive* transmission	$0 < \mathscr{T}_w(s) < 1$
A_{eff}	effective hybrid lens area	$A_{\mathrm{eff}} \propto \hat{P}_{m_i} \times \mathscr{T}_w(s)$
ΔE	absolute spectral width	$[\Delta E] = \mathrm{eV}$ or keV

Table 22 Focal plane characteristics.

Symbol	Description	Usage or (unit)
$\varnothing_{\mathrm{PSF}}$	focal spot size (HEW)	$[\varnothing_{\mathrm{PSF}}] = \mathrm{mm}$
$\Delta\epsilon_{\mathrm{coh}}$	coh. angular resolution	$\Delta\epsilon_{\mathrm{coh}} = \alpha\lambda R^{-1}$
$\Delta\epsilon_{\mathrm{inc}}$	incoh. angular resolution	$\Delta\epsilon_{\mathrm{inc}} = \varnothing_{\mathrm{PSF}}/F$
n_{FOV}	#(resolution elements)	$n_{\mathrm{FOV}} \lesssim 10^3$
r_{FOV}	detector radius	$r_{\mathrm{FOV}} = \frac{n_{\mathrm{FOV}}}{2} \varnothing_{\mathrm{PSF}}$
Δz_0	focal depth of field (DOF)	$\Delta z_0 = \pm\lambda/2(\mathrm{NA})^2$

Table 23 Modeling of observations.

Symbol	Description	Usage or (unit)
$\bar{n}_s, \bar{n}_b$	signal/backgr. count rate	$[\bar{n}_{s,b}] = \frac{1}{\mathrm{cm}^2\,\mathrm{s}\,\mathrm{kev}}$
Γ	slope of XRB power law	$\bar{n}_b \propto E^{-\Gamma}$
Δt	exposure/observ. time	$\Delta t \sim (10^3 - 10^6)\ \mathrm{s}$

Acknowledgments

This work contributes to the project "Zentrum für Innovationskompetenz ultra optics," funded by the German Federal Ministry of Education and Research (BMBF) with the fund number 03Z1HN32. Financial support by the Dr. Johannes Heidenhain foundation, Traunreut (Germany), is also recognized. The authors thank Frank Haberl for providing XMM spectra as well as Joachim Trümper and Günther Hasinger for helpful discussions.

References

1. G. K. Skinner, "Diffractive-refractive optics for high energy astronomy—ii. variations on the theme," *Astron. Astrophys.* **383**, 352–359 (2002).
2. G. K. Skinner, "Design and imaging performance of achromatic diffractive-refractive x-ray and gamma-ray Fresnel lenses," *Appl. Opt.* **43**, 4845–4853 (2004).
3. G. K. Skinner, "Diffractive x-ray telescopes," *X-Ray Opt. Instrum.* **2010**, 743485 (2010).
4. P. Gorenstein, "Focusing x-ray optics for astronomy," *X-Ray Opt. Instrum.* **2010**, 109740 (2010).
5. C. Braig and P. Predehl, "Large-scale diffractive x-ray telescopes," *Exp. Astron.* **21**, 101–123 (2007).
6. C. Braig and P. Predehl, "Efficient Fresnel x-ray optics made simple," *Appl. Opt.* **46**, 2586–2599 (2007).
7. G. K. Skinner et al., "The milli-arc-second structure imager, MASSIM: a new concept for a high angular resolution x-ray telescope," *Proc. SPIE* **7011**, 70110T (2008).
8. J. Krizmanic et al., "Development of ground-testable phase fresnel lenses in silicon," *Exp. Astron.* **20**, 299–306 (2006).
9. J. Krizmanic et al., "Phase Fresnel lens development for x-ray and gamma-ray astronomy," in *Proc. 31st ICRC*, Lódz (2009).
10. C. Braig and P. Predehl, "Advanced Fresnel x-ray telescopes for spectroscopic imaging," *Exp. Astron.* **27**, 131–155 (2010).
11. C. Braig and P. Predehl, "A diffraction-limited dual-band x-ray telescope," *Proc. SPIE* **6688**, 668808 (2007).
12. C. Braig and P. Predehl, "Toward the diffraction limit with transmissive x-ray lenses in astronomy," *Appl. Opt.* **51**, 4638–4659 (2012).
13. B. X. Yang, "Fresnel and refractive lenses for x-rays," *Nucl. Instrum. Phys. Res. A* **328**, 578–587 (1993).
14. H. Dammann, "Blazed synthetic phase-only holograms," *Optik* **31**, 95–104 (1970).
15. M. Umbach, "Achromatische Röntgenlinsen," Ph.D. Thesis, Universitätsverlag Karlsruhe, Straße am Forum 2, 76131 Karlsruhe, Germany (2009).
16. N. R. Pereira, E. M. Dufresne, and D. A. Arms, "Large aperture x-ray refractive lens from lithium," *AIP Conf. Proc.* **879**, 985–988 (2007).
17. A. Timmann et al., "Small angle x-ray scattering with a beryllium compound refractive lens as focusing optic," *Rev. Sci. Instrum.* **80**, 046103 (2009).
18. American Elements, Los Angeles, CA, http://www.americanelements.com (2012).
19. Goodfellow GmbH, 61213 Bad Nauheim, Germany, http://www.goodfellow.com (2012).
20. D. Attwood, *Soft X-rays and Extreme Ultraviolet Radiation—Principles and Applications*, Cambridge University Press, New York (1999).
21. E. M. Dufresne et al., "Lithium metal for x-ray refractive optics," *Appl. Phys. Lett.* **79**, 4085–4087 (2001).
22. D. A. Arms et al., "Refractive optics using lithium metal," *Rev. Sci. Instrum.* **73**, 1492–1494 (2002).
23. L. Coyle, "Beryllium: properties and applications – introduction to opto-mechanical engineering," http://www.optics.arizona.edu (2012).
24. R. A. Paquin, "Hot isostatic pressed beryllium for large optics," *Proc. SPIE* **0571**, 259–266 (1986).
25. J. P. Gardner et al., "The James Webb space telescope," *Space Sci. Rev.* **123**, 485–606 (2006).
26. J. Krizmanic, G. Skinner, and N. Gehrels, "Formation flying for a Fresnel lens observatory mission," *Exp. Astron.* **20**, 497–503 (2006).
27. L. Strüder et al., "Large-format, high-speed, x-ray pnCCDs combined with electron and ion imaging spectrometers in a multipurpose chamber for experiments at 4th generation light sources," *Nucl. Instrum. Methods Res. A* **614**, 483–496 (2010).
28. S. R. Bandler et al., "Performance of TES x-ray microcalorimeters with a novel absorber design," *J. Low-Temp. Phys.* **151**, 400–405 (2008).
29. S. R. Bandler et al., "Performance of high-resolution, micro-fabricated, x-ray magnetic microcalorimeters," *AIP Conf. Proc.*, **1185**, 579–582 (2009).
30. X. Barcons, D. Lumb, and R. Fraga-Encinas, "IXO—Revealing the physics of the hot Universe," Scientific study report, ESA Publications Division, Netherlands (2011).
31. Generation-X Vision Mission, Harvard-Smithsonian Center for Astrophysics, http://www.cfa.harvard.edu/hea/genx.html (2012).
32. P. J. Schields et al., "Overview of polycapillary x-ray optics," *Powder Diffrac.* **17**, 70–80 (2002).
33. IFG—Institute for Scientific Instruments GmbH, Rudower Chaussee 29/31, Berlin, Germany, http://www.ifg-adlershof.de (2011).
34. C. Kronberg, *The Munich Astro Archive*, http://www.maa.mhn.de/StarDate/bright_stars.html (2012).
35. R. Johnston, *List of Black Hole candidates*, http://www.johnstonsarchive.net/relativity/bhctable.html (2012).
36. Chandra Supernova Remnant Catalog, http://snrcat.cfa.harvard.edu/ (2012).
37. D. A. Green, *Galactic SNRs: Summary Data*, http://www.mrao.cam.ac.uk/surveys/snrs/snrs.data.html (2012).
38. *XJET: X-ray emission from extragalactic radio jets*, http://hea-www.harvard.edu/XJET/index.cgi (2012).
39. *Temperatures of cooling neutron stars*, http://www.astroscu.unam.mx/neutrones/NS-Data/data_good.dat (2012).
40. M. H. van Putten and T. Regimbau, "Observational evidence for a correlation between peak luminosities and beaming in gamma-ray bursts," *Astrophys. J.* **593**, L15 (2003).
41. I. F. Mirabel, "Jets in supermassive and stellar-mass black holes," astro-ph/0302195 (2003).
42. M. Revnivtsev et al., "The spectrum of the cosmic x-ray background observed by RXTE/PCA," *Astron. Astrophys.* **411**, 329–334 (2003).
43. G. Davis, R. Estes, and S. Glubke, "Micro arcsecond x-ray imaging mission, pathfinder (MAXIM-PF)—propulsion," NASA Goddard Space Flight Center, http://maxim.gsfc.nasa.gov/documents/MAXIM-Documents.html (2002).
44. J. Giesen, *Angular Distance of the Nearest Neighbor*, http://www.jgiesen.de/BrightStars/index.html (2012).
45. T. Shanks et al., "The origin of the cosmic x-ray background," *Nature* **353**, 315–320 (1991).
46. J. Kirz, "Phase zone plates for x rays and the extreme UV," *J. Opt. Soc. Am.* **64**, 301–309 (1974).
47. E. Di Fabrizio et al., "High-efficiency multilevel zone plates for keV x-rays," *Nature* **401**, 895–898 (1999).

Christoph Braig received his Diploma degree in physics in 2001 and his PhD degree in astronomy from the University of Munich (LMU), Germany, in 2006. After doctoral and post-doctoral research at the Max-Planck-Institut für extraterrestrische Physik (MPE) in Garching, Germany, and teaching and management activities at the LMU, he is currently a post-doc scientist with the Institute of Applied Physics and the Abbe School of Photonics at the University of Jena. His research interests include the development of diffractive optics for the EUV and x-ray band.

Peter Predehl received his Diploma degree in physics from the University of Erlangen, Germany, in 1977 and his PhD degree in physics from the University of Erlangen, Germany, in 1980. He has worked since then with the Max-Planck-Institut für extraterrestrische Physik in Garching, Germany, and has been involved in numerous space projects for x-ray astronomy. He is currently the principal investigator of the German x-ray observatory eROSITA, planned for launch in 2014.